Development of Vehicle Dynamics Control for Wheel-Motored Vehicles

By

Scott Julian Varnhagen
B.Sc. (University of Alberta) 2009
M.Sc. (University of California, Davis) 2011

DISSERTATION

Submitted in partial satisfaction of the requirements for the degree of

DOCTOR OF PHILOSOPHY

in

MECHANICAL AND AEROSPACE ENGINEERING

in the

OFFICE OF GRADUATE STUDIES

of the

UNIVERSITY OF CALIFORNIA

DAVIS

Approved:

Donald L. Margolis (Chair)

Dean C. Karnopp

Francis F. Assadian

Committee in Charge
2014

ProQuest LLC.
789 East Eisenhower Parkway
P.O. Box 1346
Ann Arbor, MI 48106 - 1346

I dedicate this work to my loving and supportive wife, Heather.

Contents

Scott Varnhagen
December 2014
Mechanical and Aerospace Engineering

Development of Vehicle Dynamics Control for Wheel-Motored Vehicles

Abstract

This dissertation describes a methodology for the vehicle dynamics control of a wheel motored vehicle. All theory is developed assuming that the driver has control of the front wheel steering angle, and that wheel torque is solely generated by independent wheel motors at each corner of the vehicle. Theoretical work is presented for the general case with four independent wheel motors, but can be easily reduced to a situation with only two wheel motors. Indeed, all theory developed in this work is evaluated experimentally on a production automobile converted to be driven by two independent rear wheel motors.

As opposed to directly allocating wheel torques, the proposed philosophy operates in the slip-ratio domain. Doing so helps to prevent excessive tire saturation and allows the system to adapt to changing road surfaces. To that end, this dissertation first proposes a method of estimating slip-ratio utilizing only sensors currently available on modern automobiles. A slip-ratio controller is then developed approximating the disturbance observer structure. This allows the controller to be robust to changing road surface and as a byproduct provide an accurate estimate of longitudinal tire force. Combining the estimated longitudinal tire force with the estimated slip-ratio it is then possible to ascertain some degree of tire saturation. With this in mind, an optimal control allocation problem is proposed which attempts to achieve the desired vehicle dynamics while at the same time minimizing tire saturation.

It is shown experimentally that the proposed control methodology effectively achieves desired vehicle dynamics. In addition, the system adapts its behavior to changing road surfaces resulting in optimal performance regardless of operating conditions.

Acknowledgments and Thanks

First and foremost, I would like to thank my academic advisor, Professor Donald Margolis. In addition to his astute guidance of this work, he has been an excellent life counselor throughout my stay at UC Davis. It has been an absolute pleasure to consult with such a kind and experienced engineer.

In addition I would like to extend sincere gratitude to my industry advisor at Ford Motor Company, Ming Kuang. It is a direct result of Ming's encouragement and support that I enrolled in the doctoral program at UC Davis in the first place. His big picture vision and guidance helped steer the project towards its final state, of which we are all proud. He went to bat for me many times, securing two valuable internships with Ford Motor Company as well as the opportunity to conduct experimental testing on a Ford research vehicle in Europe.

I would also like to thank Marcus Kalabis and Roger Graff of Ford of Europe for their attentive support throughout the project. I would especially like to thank them for their kindness and major involvement during vehicle testing in Europe.

I also express my sincere appreciations to all members of my doctoral committee: Prof. Karnopp, Prof. Assadian, Prof. Eke, Prof. Hess and Dr. Hai Yu for their valuable suggestions with regard to my doctoral research. Finally, I would like to thank the Mechanical and Aerospace Engineering faculty and staff, without whom none of this work would have been possible.

Chapter 1

Introduction

1.1 Background and Motivation

Electrified vehicle powertrains are becoming prevalent due to their high efficiency and capability of utilizing fuel sources alternative to petroleum. These electrified powertrains can be configured so that electric motors independently drive both front wheels, both rear wheels, or even all four wheels. Such a configuration is termed a wheel motored vehicle. This can be accomplished by mounting the electric motors to the sprung mass and transferring their power via conventional axle shafts, or by mounting the electric motors directly to the unsprung mass, termed a hub-electric motor. Regardless of the configuration adopted, the use of independent electric wheel motors not only allows for improvements in vehicle efficiency, but has the potential to revolutionize active handling and safety control.

Motor vehicle accidents claim more than 30,000 lives each year in America. In addition to loss of life, motor vehicle accidents cost the American economy $41 billion in medical and work loss costs alone [1]. To combat these alarming statistics a technology termed Electronic Stability Control (ESC) has been developed to help drivers maintain control of vehicles during emergency maneuvers. In essence, ESC utilizes on board wheel speed, body acceleration and yaw-rate sensors to ascertain whether the vehicle is operating in a stable domain. If the

ESC system concludes that the planar vehicle dynamics are becoming unstable, it intervenes with controlled actuation to stabilize the vehicle. A study conducted by the National Highway Traffic Safety Administration (NHTSA) concluded that ESC reduced fatal run-off-road crashes in passenger vehicles by 36% and rollover involvement in fatal crashes of passenger vehicles by 70% [2]. As a result of the efficacy indicated by this study, the NHTSA has mandates that all light vehicles produced for the American market must come equipped with ESC by model year 2012 and onward. The NHTSA projects that this mandate will prevent 5,300-9600 fatalities annually [3].

Traditionally, ESC interventions are actuated by reducing engine power and modulating individual electro-hydraulic brakes [4]. Compared with these conventional actuators, the electric wheel motor presents the following merits:

- Electric motors can generate both driving and braking torque which allows for the generation of maximum yaw-moment without impacting longitudinal velocity [5]. Conversely, conventional ESC interventions result in rapid deceleration of the vehicle which is intrusive during performance driving. For this reason, conventional ESC systems are aggressively employed only after the potential for instability is detected. The ability of a wheel motored vehicle to generate yaw-moment without effecting longitudinal velocity can allow for the electric motor's incorporation in the performance handling of the vehicle, as well as in its stability control.

- Electric motors can respond 10 times more quickly than electro-hydraulic brake systems [6].

- Unlike electro-hydraulic brake and engine systems, the torque output by the electric motor can be estimated with high accuracy [6]. This final merit is extremely beneficial as it can provide additional information regarding the interaction between the vehicle's tires and the road surface.

These merits provide a vehicle driven by wheel motors the potential to outperform conventional vehicles in both stability and handling. Improved stability performance will further improve the efficacy of ESC and reduce the human and capital costs associated with automobile accidents. Improved handling performance will make wheel motored vehicle more enjoyable to drive than conventional vehicles, hopefully increasing their rate of adoption in the market place. However, to realize this potential requires appropriate control of the wheel motors.

1.2 Research Goals

It is the goal of this research to propose realizable methodology for the control of wheel motored vehicles. This methodology should take advantage of the merits of wheel motors, resulting in a vehicle which outperforms conventional vehicles in both performance handling and stability.

As will be expounded in this work, the most notable difference between conventional powertrains and the wheel-motored powertrain is the ability to estimate with high accuracy the amount of torque being generated at a given wheel. It is proposed that this estimated torque input can be leveraged to ascertain information relating to interaction between the tire and the road surface. It is a goal of this research to demonstrate that it is possible to estimate the tractive capacity of a given tire operating on varying road surfaces in real time.

Intuitively, a driver's behavior should change with changing road surfaces. For example, it is necessary to reduce throttle/brake commands on icy surfaces to avoid saturating the tires and sliding the vehicle. It then follows that the control methodology developed in this work should adapt its behavior based on estimated road surface condition. It is a goal of this research to demonstrate that this adaptation results in desirable vehicle performance, regardless of road surface condition.

In general the development of control theory is undertaken in the mathematical domain.

Differential equations representing modeled dynamics of physical systems are analyzed, and mathematical controllers are developed in order to drive the output of these modeled equations to those desired by the user. All controllers/estimators should adhere to theoretically motivated rules for stability, robustness and optimality. It is a goal of this research to demonstrate these attributed with the necessary mathematical rigor for controllers/estimators developed in this work.

However, it is not the intention of the practical engineer to control differential equations but instead to develop methodologies to drive physical system performance towards tractable goals. To this end, it is an overarching goal of this research to ensure that all control theory developed herein is practically implementable utilizing sensors, processors and actuators currently available on modern automobiles. The tantamount goal of this work is to apply the developed theory to a physical vehicle and demonstrate the potential of wheel motors during real world operation.

1.3 Main Contributions

This dissertation presents a methodology for the vehicle dynamics control of wheel-motored vehicles. The contributions of this research are:

1. Development of a planar vehicle state estimation routine which utilizes sensors currently installed on modern automobiles. This contribution is novel as it:

   a) Incorporates rigid-body dynamics to ensure accurate estimates during vehicle cornering maneuver, and

   b) Utilizes fuzzy-membership to prescribe the validity of wheel-speed measurements with respect to torque input.

2. Applying a Controller Output Observer for the estimation of longitudinal tire force. When combined with estimated tire slip-ratio, this results in the development of a metric for the current level of tire saturation.

3. Implementing a Disturbance Observer for the control of tire slip-ratio.
4. Applying an optimal control allocation technique for the actuation of planar virtual forces. This contribution is novel as it:
    a) Allows for adaptation to changing road surface, and
    b) Proposes a sub-optimal but practically implementable control allocation problem.

All contributions are theoretically justified as well as validated with rigorous simulation and experimental study.

1.4 Guide to this Dissertation

This dissertation is organized as follows: Chapter 2 describes the proposed big picture control architecture and introduces the tasks of slip-ratio estimation, slip-ratio control as well as slip-ratio allocation. These three modules are then discussed in-depth in Chapters 3, 4 and 5 respectively. Concluding remarks as well as future research directions are then presented in Chapter 6.

Chapter 2

Proposed Control Architecture

2.1 Conventional Vehicle Control

In a conventional vehicle the driver commands vehicle performance through the use of accelerator/brake pedals as well as the steering wheel. The accelerator/brake pedal most strongly relate to the desired longitudinal acceleration of the vehicle, while the steering wheel effects heading as well as lateral acceleration. However, during overly aggressive maneuvers or operation on slippery surfaces the vehicle does not perform as expected. For example, an accelerator pedal input on an icy surface may result in the spinning of the wheels as opposed to the expected forward acceleration of the vehicle. Similarly, a large steering input near the limits of vehicle traction may result in the sliding or even spinning out of the vehicle as opposed to the expected heading adjustment.

To help mitigate these issues and improve vehicle safety modern automobiles are equipped with active safety features such as Traction Control (TC), Anti-Lock Brake systems (ABS) as well as Electronic Stability Control (ESC). Each system is tasked with intervening against a specific form of vehicle misbehavior. Specifically, TC is solely responsible for decreasing powertrain torque if wheel spin is detected during vehicle acceleration. The ABS system is responsible for modulating individual brake pressures if wheel lock-up is detected during vehicle braking. The ESC system is responsible for correcting vehicle yaw-rate if it differs largely from the desired yaw-rate by actuating the brake system at individual corners of the vehicle. In essence, three mutually exclusive control systems are implemented to correct for abnormal behavior in vehicle acceleration/braking/cornering performance.

In practice this misbehavior may not be mutually exclusive. For example, a spirited driver may wish to corner and accelerate on a slippery surface. In this situation both the vehicle's yaw-rate as well as longitudinal acceleration will differ from those desired by the driver, requiring intervention from both the ESC and TC system. However, these systems have been developed for exclusive operation and must be implemented exclusively to avoid conflicting actuator requests. To this end, the three systems are implemented via a hierarchy where the ESC system is generally awarded the highest priority. Thus, in the example situation the ESC system would be activated, actuating individual brakes to help correct the vehicle's yaw-rate. This intervention, although helping to achieve the driver's heading goals, has the unintended consequence of decelerating the vehicle in direct conflict with the driver's desire.

Conventional vehicles employ ESC to actuate the brake and powertrain systems to achieve desired lateral dynamics. Only if these lateral dynamics are within the desired threshold may the longitudinal dynamics of the vehicle be considered through the use of TC and ABS systems. The advent of the wheel-motored vehicle prompts a shift in this conventional paradigm. As the wheel-motor can generate both positive and negative torque, ESC interventions can be achieved without necessitating vehicle deceleration as was the case with conventional brake based systems. Indeed, the lateral and longitudinal dynamics of the vehicle can be controlled cooperatively with the wheel-motored vehicle, resulting in a safer and more enjoyable driving experience. This work proposes a global chassis controller which takes advantage of the merits of wheel motors to concurrently achieve the longitudinal and lateral dynamics desired by the driver.

2.2 Proposed Control Architecture

The proposed control architecture for a wheel-motored vehicle is shown in Figure 2.2.1. This architecture is relevant for a vehicle with wheel motors actuating both front wheels, both rear wheels or even all four wheels. The subscripts ij represent an individual corner of the vehicle, where $ij \in \{lf, rf, lr, rr\}$. It is assumed in this work that the driver has exclusive control over the steering angle of the front wheels, and that the rear wheels are fixed in a forward direction. The only actuators accessible to the controller are the torques delivered by the independent wheel-motors.

2.2.1 Reference Model

The reference model is critically important in the design of a control system. It is responsible for generating desired system performance based on inputs from the user. In this structure, the reference model accepts the steering wheel angle δ and accelerator/brake pedal position P_{pedal} inputs from the driver and outputs the desired yaw-rate ω_{y_d} and change in longitudinal velocity $\dot{V}_{x_d}$. The desired performance of a vehicle is often a largely proprietary trait, allowing a specific vehicle model to achieve a certain “feel”.

The development of a reference model is not the focus of this work. In general, in this work the desired yaw-rate is characterized by the 2-Degree-of-Freedom bicycle model for a slightly understeering vehicle [7]. This model is desirable as it is simple to evaluate and remains stable regardless of vehicle speed. It important to note that their are many alternative methods to developing a reference signal for stability control, including sideslip control and combined yaw-rate and sideslip control [4]

2.2.2 Reference Tracking Controller

The objective of the reference tracking controller is to minimize the error between the desired vehicle performance ($\dot{V}_{x_d}$, ω_{y_d}) and the estimated/measured vehicle performance ($\dot{V}_x$, ω_y).

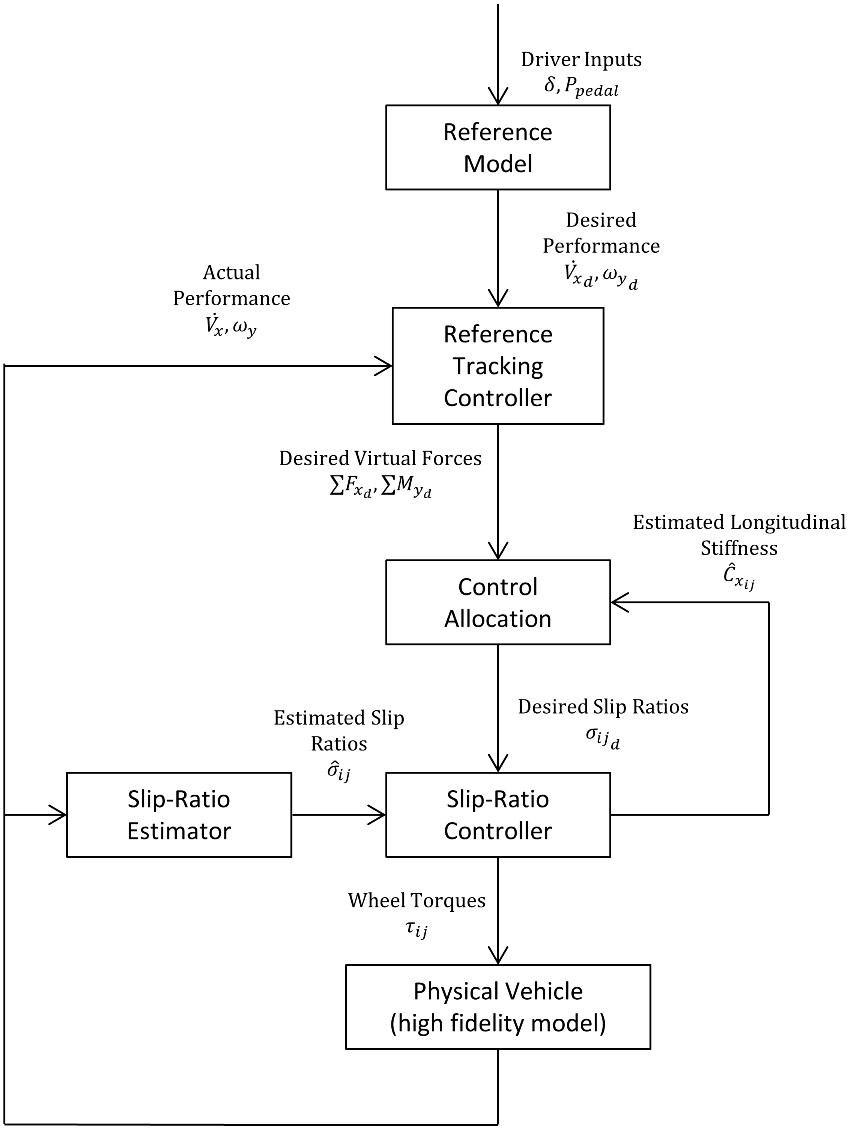

Figure 2.2.1: Block-Diagram of Proposed Control Architecture

Change in longitudinal velocity $\dot{V}_x$ is estimated as discussed in Chapter 3 and yaw-rate ω_y is measured by a gyroscopic sensor installed on modern automobiles. The reference tracking controller drives the actual vehicle performance towards the desired vehicle performance by modulating generalized virtual forces. Any controller capable of robustly driving error towards zero can be considered. This work will utilize proportional-integral control, however non-linear controllers such as sliding mode control have also been applied effectively [8].

2.2.3 Control Allocation

The two generalized virtual forces requested by the reference tracking controller are total longitudinal force ΣF_x and total yaw-moment ΣM_y. The term *generalized* is used to imply that not all terms are strictly in the force domain. For example, the sum of moments, ΣM_y, is in the torque domain. Additionally, the term *virtual* is used as no actuator exists to directly impart these generalized forces on the vehicle. Instead, they will be generated indirectly by appropriately modulating the motor torques at the corners of the vehicle, resulting in augmented tire forces. This topic will be briefly introduced in this section, with an in-depth discussion presented in Chapter 5 as well as in Reference [9].

The most significant forces affecting planar vehicle dynamics are those generated by the tires. For each tire, these forces can be decomposed into a longitudinal component F_x and a lateral component F_y. Figure 2.2.2 shows this decomposition on a free-body-diagram of the planar vehicle. The vehicle is modeled as a rigid body with three body-fixed states: longitudinal velocity V_x, lateral velocity V_y and yaw-rate ω_y. The center of gravity of the body is centered between the vehicle's trackwidth, indicated by parameter $\frac{w}{2}$.

It is our goal to augment tire forces to generate the two generalized virtual forces requested by the reference tracking controller. For simplicity, we will assume small steering angles and employ the small angle identities $\cos\delta \approx 1$ and $\sin\delta \approx 0$. To that end, we can generate a total longitudinal force by summing forces in the direction of longitudinal motion as

$$\Sigma F_x = F_{x_{lf}} + F_{x_{rf}} + F_{x_{lr}} + F_{x_{rr}} \tag{2.2.1}$$

Again, assuming small steering angles, the total yaw moment can be generated by summing moments in the direction of yaw-rate as

$$\Sigma M_y = \frac{w}{2}(F_{x_{rf}} + F_{x_{rr}} - F_{x_{lf}} - F_{x_{lr}}) \tag{2.2.2}$$

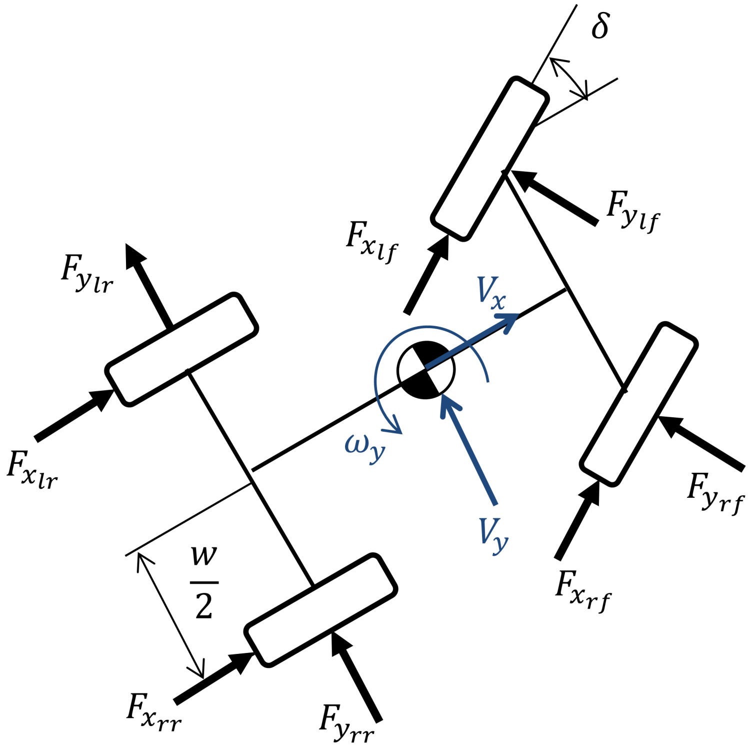

Figure 2.2.2: Planar Vehicle Free-Body-Diagram

We have shown that the desired virtual forces requested by the reference tracking controller can be achieved by intelligently augmenting the longitudinal force generated at each tire. However, as will be described subsequently, direct allocation of longitudinal force could have unintended consequences due to the nonlinear relationship by which tires generate force. For this reason, the control allocation problem is to determine which slip-ratios should be desired at each wheel to best achieve the virtual forces requested by the reference tracking controller. These desired slip-ratios are then tracked by the slip-ratio controllers discussed in Section 2.2.5.

Tire Force Generation

As tires are elastomeric, there is a strong correlation between the amount of longitudinal force generated by a tire and its deformation in the longitudinal direction. A tire's longitudinal deformation is characterized by slip-ratio σ, defined as

$$\sigma = \frac{R \cdot \omega - V_w}{\max\left(V_w, R \cdot \omega\right)} \tag{2.2.3}$$

where V_w is the longitudinal velocity of the wheel center, R is some mean radius of the wheel and ω is its angular velocity. Slip-ratio measures the difference between tire velocity $R \cdot \omega$ and wheel center velocity V_w, normalized by the maximum of the two. A spinning tire attached to a motionless chassis is characterized by a slip-ratio of $\sigma = 1$, while a locked up tire attached to a moving chassis is characterized by a slip-ratio of $\sigma = -1$.

Figure 2.2.3 presents the constitutive relationship by which tires generate longitudinal force with respect to slip-ratio. The longitudinal forces presented in this figure have been normalized by the tire's normal force F_z. For illustrative purposes, the figure highlights this relationship for tires operating on three different road surfaces, with maximum coefficient of friction $\mu_{max} = 0.2, 0.5$ and 0.8 corresponding to icy pavement, wet pavement and dry pavement respectively. As is evident in the figure, all three tires generate force in approximately linear proportion to slip-ratio when operating at relatively small slip-ratios. However, as slip ratio increases beyond this linear region the tire begins to progressively slip on the road surface and force generation saturates. This saturation occurs earlier for tires operating on lower friction surfaces.

Figure 2.2.4 shows the longitudinal force generation with respect to slip-ratio relationship for a hypothetical tire. Due to the nonlinear constitutive behavior of the tire, it can generate $2500N$ of longitudinal force operating in states $\star$ as well as $*$, as annotated on the figure. It is desirable to operate with slip-ratios at or below the slip-ratio corresponding to maximum force generation, subsequently termed σ_{max}. Operating with larger slip-ratios results in a reduction in longitudinal and lateral force generation and accelerated tire degradation. For these reasons slip-ratio should be controlled to remain at or below σ_{max}. Thus, saturated operating state $*$ should be avoided. Unfortunately, the value of σ_{max} changes dynamically

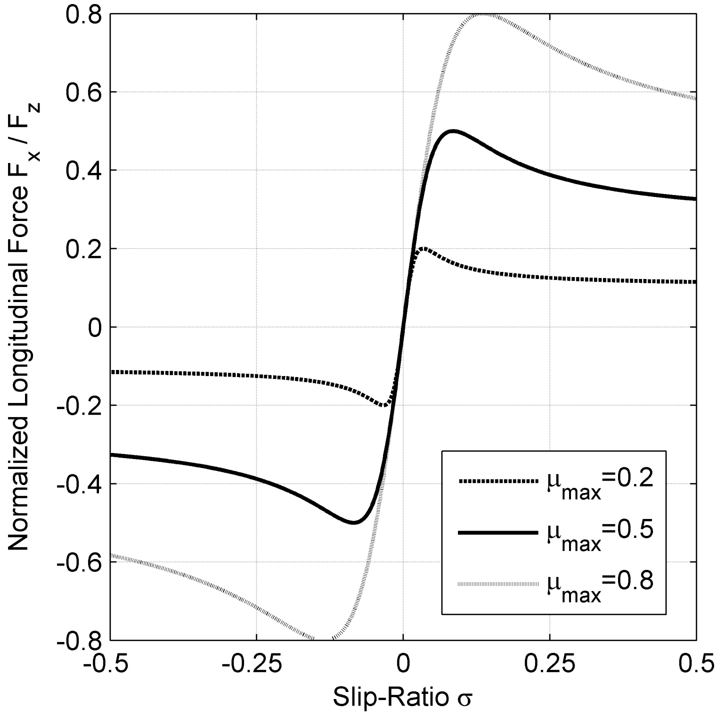

Figure 2.2.3: Normalized Longitudinal Tire Force Generation with Respect to Slip-Ratio for Tires Operating on Varying Road Surfaces

with factors such as road surface, tire wear, slip angle and normal loading [10] and as such is indeterminate during vehicle operation. Instead, the longitudinal tire stiffness, defined as

$$C_x = \frac{F_x}{\sigma} \tag{2.2.4}$$

can be used to avoid operating in a saturated state. Both slip-ratio σ and longitudinal force F_x can be estimated with high accuracy as will be discussed in Chapters 3 and 4 respectively. With these estimates, longitudinal stiffness C_x can be straightforwardly determined during vehicle operation utilizing Eqn. 2.2.4. As is evident in Figure 2.2.4, $C_x : *$ for the saturated tire is notably smaller than $C_x : \star$ for the tire operating within the linear region of force generation. As will be shown in Chapter 5, penalizing the allocation of slip-ratio to tires with lower estimated C_x results in improved vehicle performance.

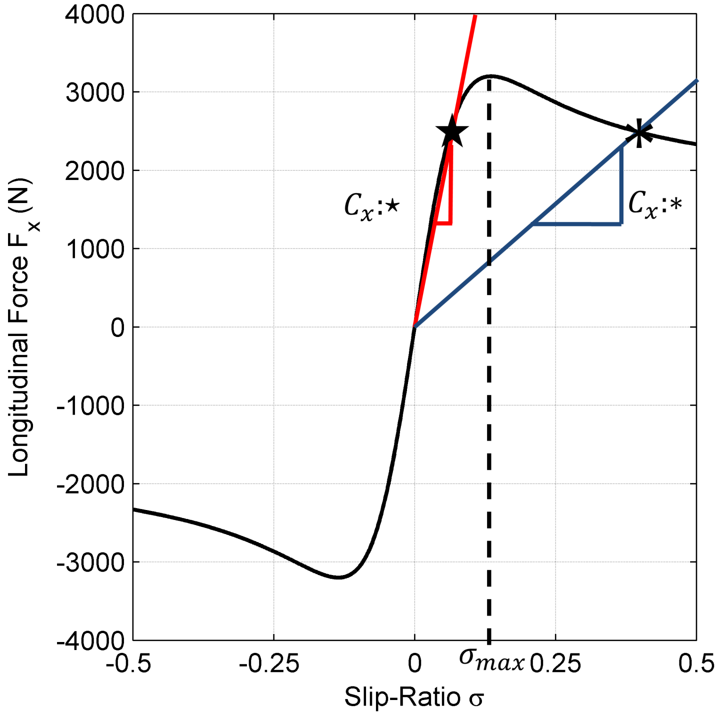

Figure 2.2.4: Longitudinal Tire Force Generation with Respect to Slip-Ratio

Assuming that slip-ratio has been constrained at or below σ_{max}, the following relationship for force generation can be used

$$F_x = C_x \sigma \tag{2.2.5}$$

Eqn. (2.2.5) in conjunction with Eqns. (2.2.1) and (2.2.2) are formulated as an optimization problem. The objective of this problem is to select the desired slip-ratios σ_{ij} which will best achieve the desired generalized virtual forces ΣF_x and ΣM_y.

2.2.4 Slip-Ratio Estimation

It was argued in Section 2.2.3 that control of slip-ratio has merits as opposed to direct tire force feedback control. However, slip-ratio, as introduced in Eqn. (2.2.3) cannot be directly measured. Instead, it must be estimated. Tire velocity, $R \cdot \omega$, can be formulated by multiplying measured wheel-speed ω with assumed static tire radius R. However, wheel center velocity cannot be straightforwardly measured, and must instead be estimated. Chapter 3 proposes a method of estimating planar vehicle states in order to facilitate the estimation of slip-ratio for each tire.

2.2.5 Slip-Ratio Controller

The slip-ratio controller for a given wheel is tasked with modulating wheel-motor torque in an attempt minimize the error between slip-ratio desired by control allocation and the estimated slip-ratio. As is evident in Figure 2.2.3, the constitutive relationship by which tires generate force varies greatly with road surface. For this reason, the tire longitudinal force is treated as a disturbance, and a slip-ratio controller was developed in a form similar to a disturbance observer to provide robustness against this disturbance. The result is a slip-ratio controller which performs well regardless of road surface. Additionally as a byproduct of its formulation, the slip-ratio controller provides an accurate estimate of longitudinal tire force $\hat{F}_x$. This estimate, in combination with estimated slip-ratio $\hat{\sigma}$ is used to prevent tire saturation as discussed in Section 2.2.3. A detailed discussion of the development and validation of the slip-ratio controller is provided in Chapter 4.

Chapter 3

Slip-Ratio Estimation

3.1 Planar State Estimation

Lateral and Longitudinal vehicle velocity are states of great interest for vehicle dynamics control. Together they can be used to estimate vehicle side-slip which is often used for vehicle stability control [4]. Additionally, knowledge of longitudinal velocity is necessary for estimation of tire longitudinal slip-ratio. Coarse estimation of slip-ratio is necessary as feedback for technologies such as Anti-Lock Brake (ABS) systems [11] and Traction Control (TC) systems. With advancements in vehicle dynamics control through the use of electrified powertrains, refinements in slip-ratio estimation are necessary to realize stability and handling enhancements [12] [9].

Much research effort is devoted to the estimation of vehicle state using only sensors available on modern automobiles. These sensors include longitudinally and laterally oriented accelerometers and yaw oriented gyroscopic sensors housed in the Inertial Measurement Unit (IMU) as well as wheel-speed sensors monitored by the ABS unit. Some research efforts also utilize Global Positioning System (GPS) sensors in their estimation [13]. The results are promising, however vehicle state estimation should remain active in situations where GPS satellites are not available.

Lateral velocity estimation schemes often rely upon assumed knowledge of tire parameters as well as known longitudinal velocity [14] [15]. However, tire parameters vary greatly during vehicle operation which can result in poor estimator performance. Additionally, as will be shown in this work, longitudinal velocity should be estimated in parallel with lateral velocity due to the coupling between them through rigid body dynamics.

The Reference [16] utilizes algebraic techniques for numerical differentiation and diagnosis of IMU signals. Depending on the diagnosed situation, the vehicle state estimator relies entirely on either the combined wheel speed measurement, or integration of IMU signals for the estimation of longitudinal velocity. Lateral velocity is estimated via integration of IMU signals, or assumed to be zero depending on the diagnosed situation. A simulation study showed the efficacy of the approach, however, the Boolean logic used to differentiate between smoothly varying situations could result in reduced estimator performance.

Fuzzy logic provides a useful extension of boolean logic for the description of smoothly varying phenomenon. The Reference [17] proposes the estimation of longitudinal vehicle velocity utilizing a Kalman filter with Fuzzy logic rule-based covariance entries. This technique allows for the smooth transition from reliance on wheel speed measurements to reliance on IMU signals for the estimation of longitudinal velocity. However, the proposed technique is developed for straight line estimation and would exhibit large error if applied to a cornering vehicle.

This work attempts to expand upon the ideas proposed in [16] and [17]. The estimator developed here utilizes longitudinal/lateral accelerometer and yaw-rate gyroscope signals from the IMU as well as wheel speed measurements to estimate vehicle state. Rigid body dynamics are considered, ensuring that the estimator is applicable during cornering. The estimator is structured as an Extended Kalman filter whose measurement noise covariance entries are selected via a Fuzzy membership function defined over input wheel torque. The result is a vehicle state estimator which utilizes sensor suites currently available on modern automobiles for the estimation of vehicle state, regardless of operating maneuver.

This chapter is organized as follows: Section 3.2 introduces the model of vehicle dynamics used for estimator development. Section 3.3 describes the proposed estimator structure with attention paid to observability as well as fuzzy membership. Section 3.4 presents a simulation study used to develop the fuzzy membership function and Section 3.5 provides experimental validation of the proposed estimation system. Finally, Section 3.6 provides concluding remarks.

3.2 Model Development

3.2.1 Vehicle State Equations

The vehicle is modeled in the plane as shown in Figure 3.2.1. The vehicle moves longitudinally with velocity V_x, laterally with velocity V_y and may rotate in the plane with yaw-rate ω_y. It is important to note that these three vectors are body fixed. As such, the longitudinal and lateral accelerations experienced at the vehicle's center of gravity are represented as:

$$a_{long} = \dot{V}_x - V_y \times \omega_y \tag{3.2.1}$$

$$a_{lat} = \dot{V}_y + V_x \times \omega_y \tag{3.2.2}$$

where the second term of each equation represents the Coriolis acceleration indicative of a body-fixed coordinate frame [18]. We are interested in how the longitudinal and lateral velocity evolves in time. To that end, we can utilize Euler integration to approximate the rate of change of velocity over the time increment $\Delta t = t(k+1) - t(k)$ as:

$$\dot{V} = \frac{V(k+1) - V(k)}{\Delta t} \tag{3.2.3}$$

where k and $k+1$ represent discrete samples of continuous signals separated by one control iteration. Utilizing this discretization, the evolution of planar vehicle states introduced in

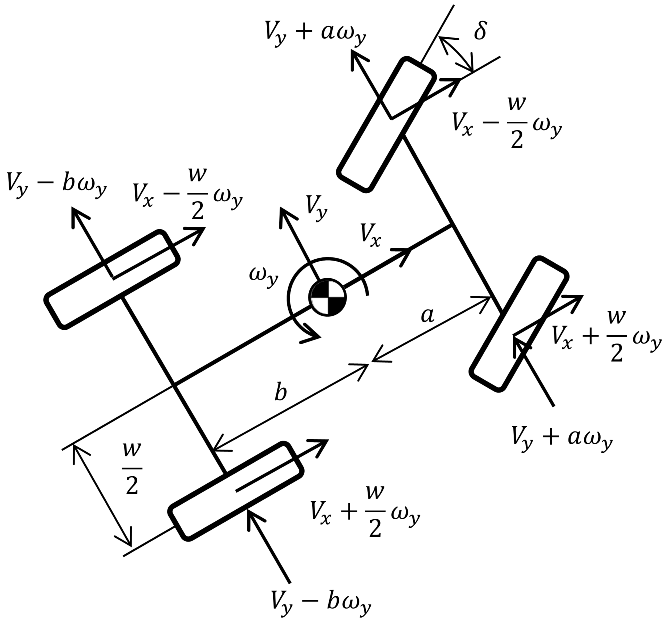

Figure 3.2.1: Velocity Diagram of Planar Vehicle

Eqns. (3.2.1) and (3.2.2), can be represented by the following finite difference equation:

$$x_{k+1} = f_k(x_k) + \boldsymbol{G}u_k \tag{3.2.4}$$

where the three planar vehicle states are contained in the state vector:

$$x_k = [V_x(k), V_y(k), \omega_y(k)]^T \tag{3.2.5}$$

with the non-linear function of states provided in Eqn. (3.2.6). Elements with subscript k denote time dependence.

$$f_k(x_k) = \begin{bmatrix} x_1(k) + \Delta t \cdot x_2(k) \cdot x_3(k) \\ x_2(k) - \Delta t \cdot x_1(k) \cdot x_3(k) \\ 0 \end{bmatrix} \tag{3.2.6}$$

The inputs to the finite difference equation (3.2.4) are measured longitudinal acceleration, lateral acceleration and yaw-rate (g_y) as packaged in the input vector:

$$u_k = [a_{long}(k), a_{lat}(k), g_y(k)]^T \tag{3.2.7}$$

These inputs are currently measured by the IMU sensor suite common on modern automobiles. It is important that IMU signals are compensated for misalignment and chassis pitch and roll angles to avoid sizable error [19] [20] when integrated over time. The input vector u_k enters the discrete state evolution equation linearly by the input matrix:

$$\boldsymbol{G} = \begin{bmatrix} \Delta t & 0 & 0 \\ 0 & \Delta t & 0 \\ 0 & 0 & 1 \end{bmatrix} \tag{3.2.8}$$

3.2.2 State Measurement Equations

Figure 3.2.1 shows the relationship between the body-fixed velocity components represented at the vehicle's center of gravity and the corresponding velocity components at the vehicle's four wheels. The vehicle's center of gravity is located by parameters $\frac{w}{2}, a$ and b. The components of the vehicle velocity at each corner of the vehicle can be projected in the direction of wheel orientation as provided in Eqns. (3.2.9)-(3.2.12).

$$V_{w_{lf}} = (V_x - \frac{w}{2}\omega_y)\cos\delta + (V_y + a\omega_y)\sin\delta \tag{3.2.9}$$

$$V_{w_{rf}} = (V_x + \frac{w}{2}\omega_y)\cos\delta + (V_y + a\omega_y)\sin\delta \tag{3.2.10}$$

$$V_{w_{lr}} = V_x - \frac{w}{2}\omega_y \tag{3.2.11}$$

$$V_{w_{rr}} = V_x + \frac{w}{2}\omega_y \tag{3.2.12}$$

Assuming that a wheel rolls freely over the ground, the aforementioned velocity components can be determined from wheel speed measurements ω and approximately known wheel radius R as follows:

$$V_{w_{ij}} = R \cdot \omega_{ij} \tag{3.2.13}$$

where $ij \in \{lf, rf, lr, rr\}$ represents the four corners of the vehicle. However, the assumption that a wheel rolls freely is easily violated with the application of wheel torque, resulting in longitudinal slip deformation of the tire. This violation is addressed in Section 3.3.3. It is assumed that the dynamic change of tire radius is negligible.

With these issues currently set aside, wheels speeds at each corner of the vehicle can be determined as a function of vehicle state as follows:

$$z_k = \boldsymbol{H}_k x_k \tag{3.2.14}$$

where z_k is the wheel velocity vector

$$z_k = [V_{w_{lf}}(k), V_{w_{rf}}(k), V_{w_{lr}}(k), V_{w_{rr}}(k)]^T \tag{3.2.15}$$

and matrix $\boldsymbol{H}_k$ is defined as

$$\boldsymbol{H}_k = \begin{bmatrix} \cos(\delta(k)) & \sin(\delta(k) & -\frac{w}{2}\cos(\delta(k)) + a\sin(\delta(k)) \\ \cos(\delta(k)) & \sin(\delta(k) & \frac{w}{2}\cos(\delta(k)) + a\sin(\delta(k)) \\ 1 & 0 & -\frac{w}{2} \\ 1 & 0 & \frac{w}{2} \end{bmatrix} \tag{3.2.16}$$

3.3 Estimator Development

3.3.1 Extended Kalman Filter

The system developed in Section 3.2 can be written with input and measurement noise as

$$x_{k+1} = f_k(x_k) + \boldsymbol{G}u_k + \boldsymbol{G}w_k \tag{3.3.1}$$

$$z_k = \boldsymbol{H}_k x_k + v_k \tag{3.3.2}$$

where

$$w_k = [w_{a_{long}}(k), w_{a_{lat}}(k), w_{g_y}(k)]^T \tag{3.3.3}$$

is the vector of noise corresponding to each of the input entries, and

$$v_k = [v_{\omega_{lf}}(k), v_{\omega_{rf}}(k), v_{\omega_{lr}}(k), v_{\omega_{rr}}(k)]^T \tag{3.3.4}$$

is the vector of measurement noise corresponding to each wheel velocity measurement. The state update equation (3.3.1) is non-linear due to the Coriolis coupling terms of Eqns. (3.2.1) and (3.2.2). However, the non-linear function $f_k(x_k)$ can be represented by a Taylor expansion about the previous state estimate $\hat{x}_{k|k}$ as

$$f_k(x_k) = f(\hat{x}_{k|k}) + \boldsymbol{F}_k(x_k - \hat{x}_{k|k}) + \mathcal{O}(||x_k - \hat{x}_{k|k}||^2) \tag{3.3.5}$$

where $\mathcal{O}(||x_k - \hat{x}_{k|k}||^2)$ represents higher order terms. Assuming that the state estimate is in the neighborhood of the true state, we neglect these higher order terms and define

$$f_k(x_k) \approx f(\hat{x}_{k|k}) + \boldsymbol{F}_k(x_k - \hat{x}_{k|k}) \tag{3.3.6}$$

where $\boldsymbol{F}_k$ is the Jacobian of function f_x, defined as

$$\boldsymbol{F}_k = \left.\frac{\partial f_k(k)}{\partial x}\right|_{x=\hat{x}_{k|k}} = \begin{bmatrix} 1 & \Delta t \hat{x}_{3_{k|k}} & \Delta t \hat{x}_{2_{k|k}} \\ -\Delta t \hat{x}_{3_{k|k}} & 1 & -\Delta t \hat{x}_{1_{k|k}} \\ 0 & 0 & 0 \end{bmatrix} \tag{3.3.7}$$

It is our goal to utilize a Kalman filter [21] to estimate the planar vehicle states, optimally fusing the input measurements u_k and output measurements z_k. Since the Kalman filter is developed for linear systems it is necessary to approximate our non-linear system as the linear system defined by

$$x_{k+1} = \boldsymbol{F}_k x_k + u_k' + w_k \tag{3.3.8}$$

where the augmented system input is given by

$$u_k' = f_k(\hat{x}_{k|k}) - \boldsymbol{F}_k \hat{x}_{k|k} + \boldsymbol{G} u_k \tag{3.3.9}$$

Together equations (3.3.8) and (3.3.2) constitute a linear system appropriate for Kalman filtering. The input and output measurement noise is assumed to be uncorrelated and white with variance defined in Eqns. (3.3.10) and (3.3.11).

$$\mathrm{E}[w_k w_j^T] = \boldsymbol{W}_k \delta_{kj} \tag{3.3.10}$$

$$\mathrm{E}[v_k v_j^T] = \boldsymbol{V}_k \delta_{kj} \tag{3.3.11}$$

The recursive Extended Kalman Filter is implemented as follows [22]. First, an a priori estimate of state, $\hat{x}_{k+1|k}$ is generated utilizing the previous estimate of state, as well as current input vector as shown in Eqn. (3.3.12). It is important to note that the a priori estimate is propagated through the non-linear state equation. Additionally, the prediction error covariance matrix is updated as shown in Eqn. (3.3.13).

$$\hat{x}_{k+1|k} = f_k(\hat{x}_{k|k}) + \boldsymbol{G}u_k \tag{3.3.12}$$

$$\boldsymbol{P}_{k+1|k} = \boldsymbol{F}_k\boldsymbol{P}_{k|k}\boldsymbol{F}_k^T + \boldsymbol{W}_k \tag{3.3.13}$$

Next, the Kalman filter gain $\boldsymbol{K}$ is updated as shown in Eqn. (3.3.14). Utilizing this gain, the a posteriori estimate of state is generated in Eqn. (3.3.15). This estimate is a combination of the a priori estimate generated in Eqn. (3.3.12) and the state estimate resulting from measurement vector z_k. The relative weighting between these two estimates is provided by the Kalman filter gain, and is the topic of discussion in Section 3.3.3. Finally, the prediction error covariance matrix is again updated as shown in Eqn. (3.3.16).

$$\boldsymbol{K}_{k+1} = \boldsymbol{P}_{k+1|k}\boldsymbol{H}_{k+1}^T[\boldsymbol{H}_{k+1}\boldsymbol{P}_{k+1|k}\boldsymbol{H}_{k+1}^T + \boldsymbol{V}_{k+1}]^{-1} \tag{3.3.14}$$

$$\hat{x}_{k+1|k+1} = \hat{x}_{k+1|k} + \boldsymbol{K}_{k+1}[z_k - \boldsymbol{H}_k\hat{x}_{k+1|k}] \tag{3.3.15}$$

$$\boldsymbol{P}_{k+1|k+1} = [\boldsymbol{I} - \boldsymbol{K}_{k+1}\boldsymbol{H}_{k+1}]\boldsymbol{P}_{k+1|k} \tag{3.3.16}$$

Equations (3.3.12)-(3.3.16) are evaluated consecutively, constituting a recursive realization of the extended Kalman filter. Assuming the vehicle starts at rest the recursion is initiated with initial state $\hat{x}_{0|0} = x_0$ and initial prediction error covariance $\boldsymbol{P}_{0|0} = \boldsymbol{0}$. It is important to note that the EKF is not the only method of applying the Kalman filter technique to non-linear systems. The Unscented Kalman Filter (UKF) and Ensemble Kalman Filter (EnKF) have also been proven for the state estimation of nonlinear systems [23]. However, as the only nonlinearity encountered in this work is simply the multiplication of two state variables by each other, the EKF and its first order Taylor series approximation is deemed sufficient.

3.3.2 Observability Criterion

The extended Kalman filter presented in the previous section relies upon the following linearized state-space system realization:

$$x_{k+1} = \boldsymbol{F}_k x_k + u'_k \tag{3.3.17}$$

$$z_k = \boldsymbol{H}_k x_k \tag{3.3.18}$$

where $\boldsymbol{F}_k$ is defined in Eqn. (3.3.7) and $\boldsymbol{H}_k$ in Eqn. (3.2.16). This linear system is said to be observable[1] if and only if the observability matrix

$$\boldsymbol{\mathcal{O}bs} = [\boldsymbol{H}_k, \boldsymbol{H}_k \boldsymbol{F}_k, ..., \boldsymbol{H}_k \boldsymbol{F}_k^n]^T \tag{3.3.19}$$

has rank n, where n is the number of system states [21]. It is found that the system model described in this work is observable for non-zero yaw rate and non-zero steering angle. However, when $\boldsymbol{F}_k$ is linearized about $\omega_y = \hat{x}_3 = 0$ and $\delta = 0$, the observability matrix drops by a rank of one, meaning that one of the three states has become unobservable. Conducting a Kalman Decomposition [24], the system may be transformed to the standard form for unobservable systems utilizing the following similarity transformation

$$\hat{\boldsymbol{F}} = \boldsymbol{T}\boldsymbol{F}\boldsymbol{T}^{-1} = \begin{bmatrix} \boldsymbol{F}_1 & \boldsymbol{0} \\ \boldsymbol{F}_{21} & \boldsymbol{F}_2 \end{bmatrix} \text{ and } \hat{\boldsymbol{H}} = \boldsymbol{H}\boldsymbol{T}^{-1} = \begin{bmatrix} \boldsymbol{H}_1 & \boldsymbol{0} \end{bmatrix} \tag{3.3.20}$$

where

$$\boldsymbol{T} = \begin{bmatrix} 1 & 0 & 0 \\ 0 & 0 & 1 \\ 0 & 1 & 0 \end{bmatrix} = \begin{bmatrix} v_{o1} & v_{o2} & v_{\bar{o}} \end{bmatrix} \tag{3.3.21}$$

---

[1] If a system is completely observable, knowledge of $\{u_k\}$ and $\{z_k\}$ for $k \in [0, n-1]$ suffices to determine x_o [21].

The pair $(\boldsymbol{F}_1, \boldsymbol{H}_1)$ is the observable portion of standard form of the unobservable system $(\hat{\boldsymbol{F}}, \hat{\boldsymbol{H}})$. In this instance, the vectors $\{v_{o1}, v_{o2}\}$ are a basis for the observable subspace and $\{v_{\bar{o}}\}$ is a basis for the unobservable subspace. It then follows that the unobservable state is lateral velocity V_y. This result can be explained intuitively by revisiting Figure 3.2.1. V_y experienced at the center of gravity is orthogonal to wheel alignment at the rear axle, and is projected onto the front axle by component $\sin(\delta)$. However, assuming small steering angles, lateral velocity is essentially orthogonal to wheel alignment at the front axle as well. The result is that V_y cannot be directly measured by wheel speed measurements z_k. Fortunately lateral velocity is coupled to the directly observed states through the kinematic relationship of Eqns. (3.2.1) and (3.2.2). Thus, for nonzero yaw-rate the lateral velocity may be indirectly observed resulting in the full rank observability matrix.

Additionally, lateral velocity at the center of gravity may be observed through the front wheels with nonzero steering angle. However, for small steering angles this observability is very weak, and noise in wheel speed measurement will be amplified into inaccurate lateral velocity estimate. For this reason it is proposed that below a certain steering angle threshold, front wheel speed measurement should be neglected in the estimation of lateral vehicle velocity utilizing the following pseudocode:

```
if $|\delta| < \delta_{threshold}$ then
    $\delta = 0$
else
    $\delta = \delta$
end if
```

where $\delta_{threshold}$ is selected by the calibration engineer.

In order to guarantee stability of the estimation algorithm, the system must be detectable[2]. Fortunately, the eigenvalue of the unobservable state is $z = 1$ corresponding to a discrete integrator. Thus, the system is detectable for all time, and bounded state estimates

---

[2] Detectability is a relaxation of observability, requiring that the dynamics of any unobservable states be stable [21].

should be expected from bounded inputs.

3.3.3 Fuzzification of Measurement Noise

As discussed in Section 3.2.2, wheel speed measurements are used to estimate the velocity of a given wheel center based on the effective tire radius using Eqn. (3.2.13). However, the wheel center velocity is not generally equal to the tire velocity due to the elastomeric properties of the tire. Instead, the two velocities are related via longitudinal tire deformation, represented by slip-ratio σ:

$$\sigma = \frac{R \cdot \omega - V_w}{\max\left(R \cdot \omega, V_w\right)} \tag{3.3.22}$$

where $R \cdot \omega$ represent the velocity of the tire and V_w represents the velocity of the wheel center. From Eqn. (3.3.22) it is evident that Eqn. (3.2.13) is only valid for slip-ratios $\sigma = 0$, and is approximately valid for very small slip-ratios.

In general, tires generate slip ratio in response to input torque from the brake and powertrain systems, subsequently denoted as τ. Thus, wheel speed measurements from a wheel subjected to significant input torque will be ineffective at predicting wheel center velocity. Conversely, the slip-ratio for a wheel subjected to minimal input torque can be assumed to be small, $\sigma \approx 0$. In this situation, wheel speed measurement can be used to reliably predict wheel center velocity.

On the other hand, automotive grade accelerometer and gyroscopic sensor signals are relatively noisy and prone to drift when compared with wheel speed measurement signals [17]. If a given wheel is operating with very little slip-ratio, the respective wheel speed measurement should be more strongly relied upon for state estimation. However, in the presence of significant input torque, the IMU signals should be more strongly relied upon. The Kalman filter structure allows for such estimation weighting through the selection of input and measurement noise covariance matrices $\boldsymbol{W}, \boldsymbol{V}$ presented in Eqns. (3.3.10),(3.3.11). As the variance of the noise inherent in the IMU measurements remains approximately constant in time, we define:

$$\boldsymbol{W} = \begin{bmatrix} n_{a_{long}} & 0 & 0 \\ 0 & n_{a_{lat}} & 0 \\ 0 & 0 & n_{g_y} \end{bmatrix} \tag{3.3.23}$$

where $n_{a_{long}}, n_{a_{lat}}$ and n_{g_y} represent the variance of the longitudinal/lateral accelerometer and yaw-rate gyroscope signals respectively. The structure of $\boldsymbol{W}$ is based on the assumption that no cross-correlation exists between the three signals. Additionally, we define the measurement variance matrix as:

$$\boldsymbol{V}_k = \begin{bmatrix} n_{w_{lf}}(k) & 0 & 0 & 0 \\ 0 & n_{w_{rf}}(k) & 0 & 0 \\ 0 & 0 & n_{w_{lr}}(k) & 0 \\ 0 & 0 & 0 & n_{w_{rr}}(k) \end{bmatrix} \tag{3.3.24}$$

where $n_{w_{ij}}$ represents the variance of respective wheel speed signals. Wheels operating with substantial input torque, τ, should be assigned a large value of n_w representing high variance in measurement noise with the converse true for free rolling wheels. Based on this sentiment, the following fuzzy rule base is proposed:

- If τ is small, then $n_w = \eta_{small}$
- If τ is large, then $n_w = \eta_{large}$

where η_{small} and η_{large} are user defined small and large constant values separated by multiple orders of magnitude. A suggested fuzzy membership function for a wheel operating with "small" input torque is provided in Figure 3.3.1. This membership functions was arrived upon via simulation and experimental study. Changing the shape of this function has a large effect on estimator performance, and should be carefully designed by the calibration engineer.

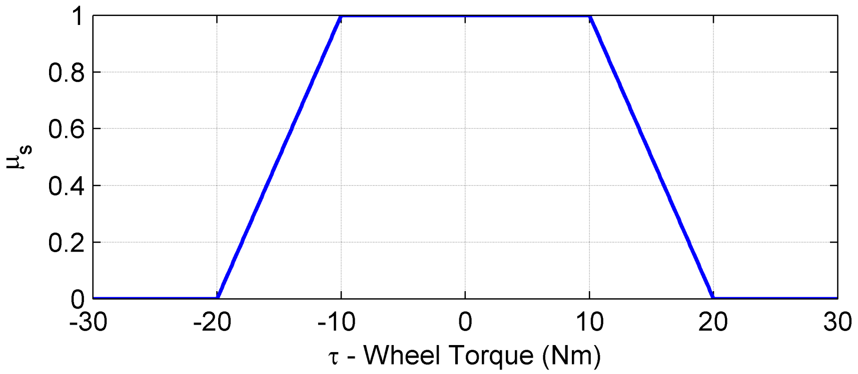

Figure 3.3.1: Membership Function for "Small" Wheel Torque

Using singleton fuzzification, product composition and inference, and centroid defuzzification [25], the expression for n_w is given by:

$$n_w(k) = \eta_{small}\mu_s(\tau(k)) + \eta_{large}(1 - \mu_s(\tau(k))) \tag{3.3.25}$$

Utilizing the adaptive measurement noise covariance matrix $\boldsymbol{V}_k$ allows the Kalman filter to smoothly adapt to changing driving situations.

3.4 Simulation Study

The Extended Kalman filter developed in this work was validated utilizing the CarSim© vehicle simulation environment. A standard B-class hatchback was simulated from an initial velocity of $80kph$ and subjected to the open-loop steering input shown in Figure 3.4.1. The purpose of this maneuver was to study the efficacy of the EKF during transient cornering. IMU and wheel speed measurements provided by CarSim© were injected with zero mean Gaussian noise with variance highlighted in Table 3.1. These variance values approximately replicate signal noise measured during production vehicle operation. The input noise covariance matrix $\boldsymbol{W}$ introduced in Eqn. (3.3.23) was populated with the same variance values as shown in Table 3.1.

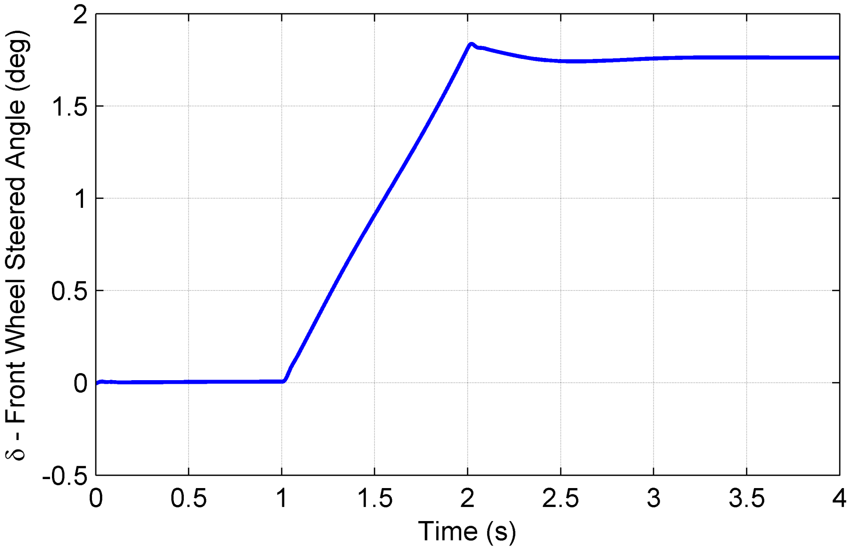

Figure 3.4.1: Open-Loop Steering Input Measured at Wheel

Table 3.1: Simulated Sensor Variance

Signal Nomenclature	Input Sensor	Variance
a_{long}	Longitudinal Accelerometer	$0.02\frac{m}{s^2}$
a_{lat}	Lateral Accelerometer	$0.02\frac{m}{s^2}$
g_y	Yaw-Rate Gyroscope	$0.002\frac{rad}{s}$
V_w	Wheel-Speed $(R \cdot \omega)$	$0.005\frac{m}{s}$

The same input torque was injected at all four wheels of the vehicle, and a batch simulation was conducted varying this value from $\tau = [-30, 30]Nm$. For each study, the planar vehicle states were estimated in three ways. The first method utilized only *Wheel-Speed* measurements, relying upon the relationship established by Eqn. (3.2.14). To extract the vehicle states from this linear measurement relationship the Moore-Penrose pseudo-inverse [24] was utilized as

$$\hat{x}_k = \boldsymbol{H}_k^+ z_k \tag{3.4.1}$$

resulting in the best estimate of vehicle state with respect to wheel-speed measurement in the least squared sense. The second method utilized to estimate planar vehicle state relied only on *IMU* signals by numerically integrating Eqn. (3.2.4). The accelerometer signals received from CarSim© were meant to mimic measurements taken by body fixed sensors, meaning that they were corrupted by the projection of gravitational acceleration during the roll and pitch action of the vehicle. Finally, the planar vehicle states were estimated utilizing the *EKF* developed in this work. The measurement variance matrix was adapted utilizing the fuzzy logic described in Section 3.3.3 with $\eta_{small} = 0.01$ and $\eta_{large} = 100$.

For each simulation study, the Mean Squared Error (MSE) for the longitudinal and lateral velocities were generated by summing the squared error between estimated velocity $\hat{V}$ and the known velocity V (reported by Carsim©) as shown in the following equation

$$V_{MSE} = \frac{1}{n}\sum_{i=1}^{n}(\hat{V} - V)^2 \tag{3.4.2}$$

where n is the total number of estimator iterations. All three estimation methods operated with a time step of $\Delta t = 0.01s$, equivalent to a frequency of $100Hz$.

Figure 3.4.2 highlights the MSE in longitudinal velocity estimation of the three methods with respect to changing input wheel torque. As is evident in the figure,the *Wheel-Speed* method of estimating longitudinal velocity was extremely accurate when the wheels were subjected to small input torques. The skewing of this relation towards positive torque is due to the rolling resistance of the tires, which was unaccounted for by the estimation model. Specifically, when operated with zero input torque the tire will still assume some small longitudinal deformation as a result of the rolling resistance encountered at the contact patch, resulting in estimation error. As expected, increasing wheel torque resulted in increased velocity estimation error. Error in longitudinal velocity estimated by the *IMU* method was also effected by wheel torque, but to a lesser extent. This trend was the result of the increased pitch motion of the vehicle experienced during larger absolute wheel torques. Stabilizing accelerometer measurements with respect to the roll/pitch motion of the vehicle could help to negate this trend [20]. Due to the increased noise of the IMU sensors as compared with the wheel-speed measurements, the *IMU* method exhibited larger estimation error for small

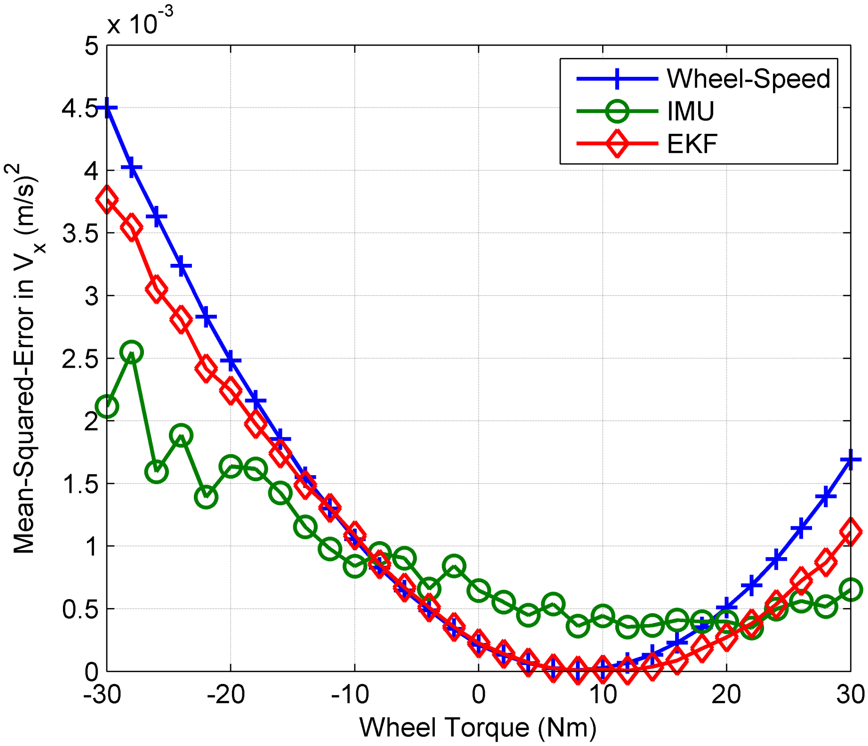

Figure 3.4.2: Mean-Squared-Error in Estimation of Longitudinal Velocity with Respect to Input Wheel Torques

wheel torques when compared with the *Wheel-Speed* method.

By utilizing fuzzy logic to adapt its measurement variance matrix entries, the *EKF* method is able to leverage the strengths of the two sensor suites to return accurate estimates of longitudinal velocity, regardless of operating state. Similarly, Figure 3.4.3 highlights the MSE in lateral velocity estimation of the three methods. Similar trends to the longitudinal velocity study can be observed. However, the MSE in the estimation of lateral velocity is generally higher than that for the estimation of Longitudinal velocity. The increased error exhibited by the *IMU* method may be attributed to lack of stabilization of accelerometer measurements with respect to the roll motion of the vehicle. Increased error exhibited by the *Wheel-Speed* method can be attributed to the poor observability of lateral velocity resulting from small front steering wheel angle discussed in Section 3.3.2. Again, the *EKF* method is able to leverage the strengths of these two sensor suites to return an accurate estimate of

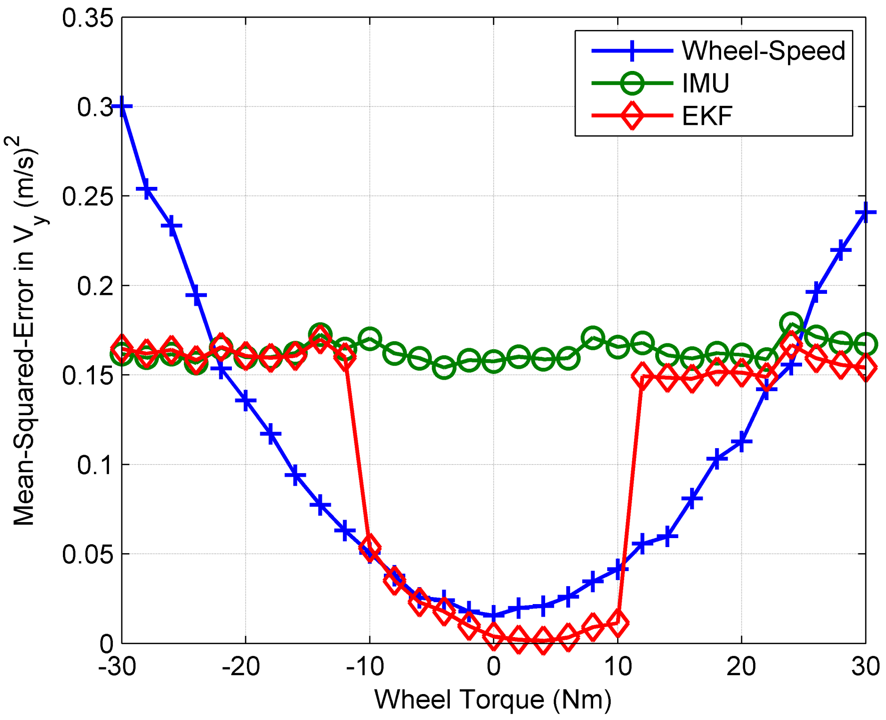

Figure 3.4.3: Mean-Squared-Error in Estimation of Lateral Velocity with Respect to Input Wheel Torques

lateral velocity, regardless of operating state.

3.5 Experimental Validation

Experimental validation was performed to study the efficacy of the planar state estimation technique proposed in this work when applied with "real-world" sensor data. A small portion of the collected data is presented, highlighting the performance of the estimator when applied to a vehicle piloting the highly dynamic handling track presented in Figure 3.5.1. A B-class production vehicle was instrumented with a Racelogic Vbox3i 100Hz GPS Data Logger. The purpose of the Vbox was to record absolute planar vehicle states to compare with the states estimated by the methods presented in this work.

All signals used by the state estimators were collected from the vehicle's Controlled Area

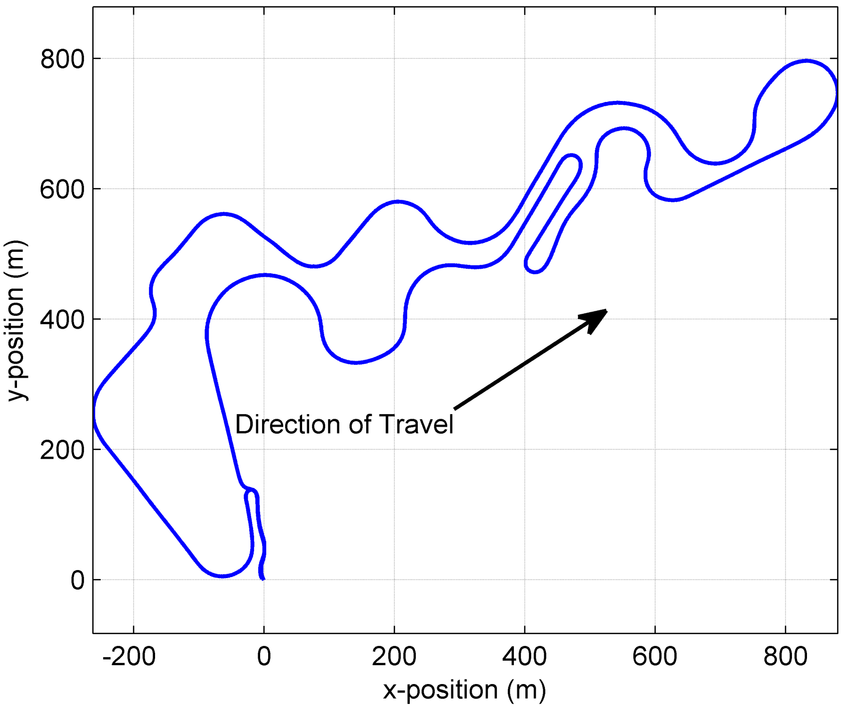

Figure 3.5.1: GPS Layout of Handling Track, Collected by Vbox Differential-GPS Sensor

Network (CAN) bus at a rate of $100Hz$. Thus, these signals are representative of production sensor and signal filtration techniques. The recorded accelerometer signals were not stabilized for vehicle pitch/roll motion which was found to be a cause of error during extreme cornering and acceleration/braking. Figure 3.5.2 compares the vehicle states estimated by the EKF with those measured by the Vbox. Unfortunately, the data acquisition system was not capable of recording the vehicle's true lateral velocity. From the figure it is evident that the estimated states show good agreement with those measured by the Vbox GPS data logger.

Table 3.2 records the Mean-Squared-Error (MSE) of longitudinal velocity estimates generated by the three techniques described in Section 3.4 compared with the longitudinal velocity measured by the Vbox. Most notably, the MSE of the *IMU* technique at estimating longitudinal velocity is orders of magnitude larger than for the other two techniques. This larger error highlights the challenge of integrating accelerometer signals for the purpose of estimating velocity. Small error in accelerometer measurement due to chassis roll/pitch, sensor

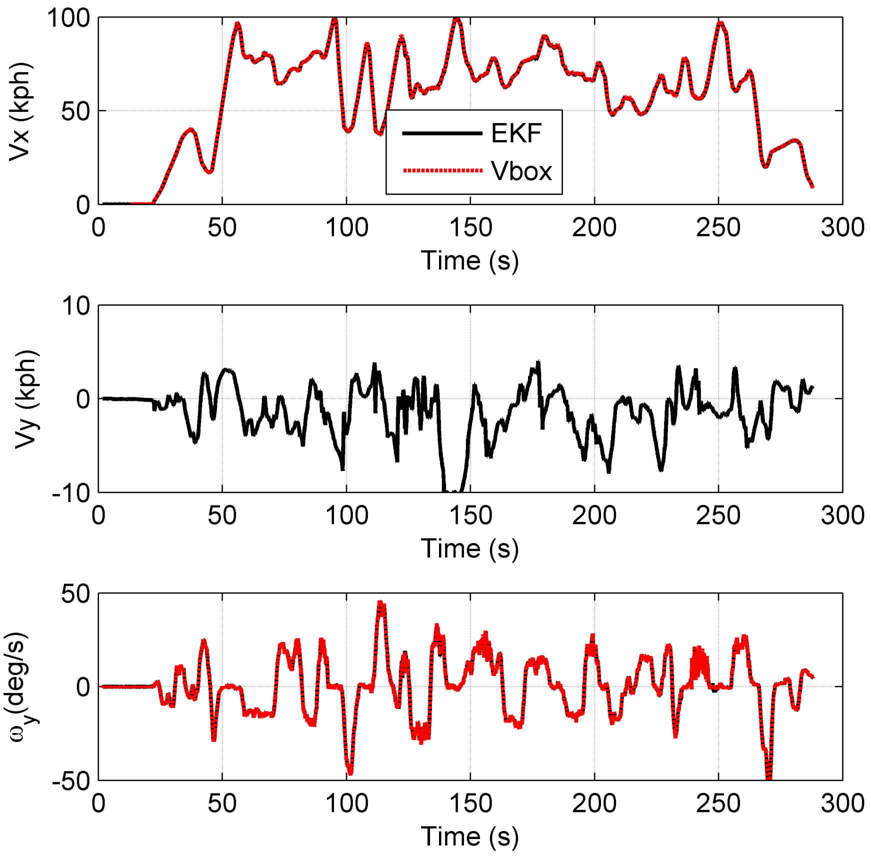

Figure 3.5.2: Extended Kalman Filter Estimated Vehicle States Compared with True Values

misalignment, road grade as well as sensor drift result in large errors in velocity estimation when integrated over time. For this reason, it is necessary to only rely upon IMU signals for velocity estimation for short time periods while wheel speed measurement is deemed unreliable.

This technique was realized utilizing fuzzy-logic, as described in Section 3.3.3. It was found that a fuzzy rule base saturating between $\eta_{small} = 0.01$, and $\eta_{large} = 10$ resulted in good EKF performance. Compared with the value $\eta_{large} = 100$ used in the simulation study, it was found that experimentally recorded IMU signals should be less strongly relied upon. Carefully stabilizing accelerometer signals for chassis pitch/roll as well as road grade could allow the IMU signals to be more strongly relied upon in future studies. From Table 3.2

Table 3.2: Mean-Squared-Error in Estimated Longitudinal Velocity

Estimation Method	MSE $(\frac{m}{s})^2$
Wheel-Speed	0.0128
IMU	32.851
EKF	0.0125

it is evident that both the *wheel-speed* and *EKF* methods estimated longitudinal velocity with little error. However, the *EKF* was able to slightly outperform the *wheel-speed* method. This performance advantage came by fusing IMU measurements with wheel-speed measurements for instances when large brake or acceleration torque was being applied, biasing the wheel-speed measurements. Improvements to the stabilization of IMU signals should further improve the efficacy of the EKF method.

Unfortunately, lateral vehicle velocity was not directly recorded by the Vbox GPS unit. It is proposed that future vehicle testing should be conducted to directly record lateral velocity and validate the EKF performance in this respect. However, the magnitude of lateral velocity evident in Figure 3.5.2 appears reasonable. To further investigate the validity of the lateral velocity estimate, the body side-slip angle β was calculated as

$$\beta = -\arctan(\frac{V_y}{V_x}) \tag{3.5.1}$$

and presented in Figure 3.5.3. These values of side-slip are commensurate with data recorded by dual antenna GPS systems in other studies [26] [27], and could provide beneficial feedback for the stability control of modern automobiles.

Slip-Ratio Estimation

For this work, the goal of planar state estimation was to facilitate the estimation of slip-ratio at each corner of the vehicle. As presented in Eqn. (3.3.22), this estimate can be extremely noisy and possible even numerically unstable for low tire/vehicle velocities. For this reason,

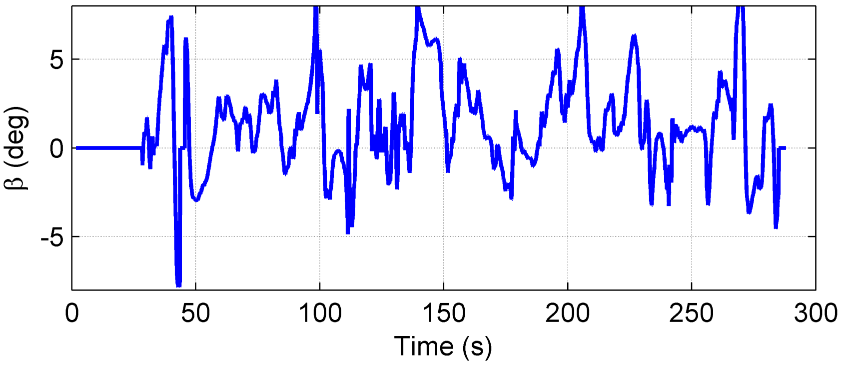

Figure 3.5.3: Extended Kalman Filter Estimated Body Side-Slip

slip-ratio is determine experimentally as

$$\sigma = \frac{R \cdot \omega - V_w}{\max\left(R \cdot \omega, V_w, \epsilon\right)} \tag{3.5.2}$$

where ϵ is a constant value to prevent division by exceedingly small numbers at low vehicle velocities. For the experimental data presented in this work $\epsilon = 30$. This large value of ϵ was required due to pragmatic limitations of the experimental vehicle being tested, and should conceivably be reduced for standard implementation. (3.5.2) compares the velocity of the tire, characterized by the wheel-speed measurement ω with the longitudinal velocity of the chassis at each respective corner of the vehicle V_w. Referring back to Figure 3.2.1 the relationship between the estimated center of gravity longitudinal velocity V_x and the longitudinal velocity experienced at each corner of the vehicle can be determined as

$$V_{w_{lf}} = V_{w_{lr}} = V_x - \frac{w}{2}\omega_y \tag{3.5.3}$$

$$V_{w_{rf}} = V_{w_{rr}} = V_x + \frac{w}{2}\omega_y \tag{3.5.4}$$

Utilizing Eqns. (3.5.3) and (3.5.4) in conjunction with Eqn. (3.5.2) the slip-ratio of each tire was estimated. A sample of these estimates is provided in Figure 3.5.4 during operation on the handling track presented in Figure 3.5.1. These estimates are commensurate with the

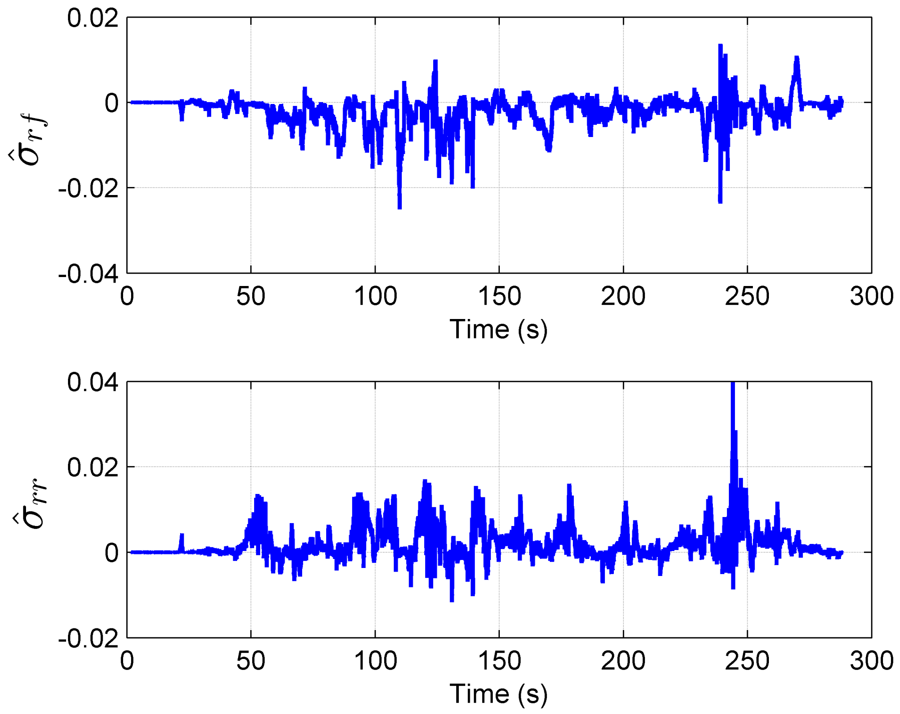

Figure 3.5.4: Extended Kalman Filter Estimated Slip-Ratios

expected values for a vehicle being driven aggressively on dry pavement.

3.6 Summary of Slip-Ratio Estimation

An Extended Kalman filter has been developed to facilitate the estimation of planar vehicle state by optimally fusing wheel-speed and IMU measurements. The body-fixed nature of the on-board IMU is modeled by the EKF allowing for accurate state estimates during cornering maneuvers. Additionally, the measurement noise covariance matrix of the filter is adapted in response to wheel torque inputs via a fuzzy inference system. The result is a vehicle state estimator capable of accurate operation during any vehicle accelerating/braking/cornering maneuver. Estimator performance was studied in the CarSim© simulation environment as well as with experimentally recorded data. In both situations it was found that the estimation philosophy proposed in this work accurately estimated vehicle state regardless of vehicle maneuver. It was shown that the estimated longitudinal velocity could be used to accurately estimate the slip-ratio of tires at each corner of the vehicle. This result is especially promising as the estimator only utilizes sensors currently installed on modern production automobiles.

Chapter 4

Control of Slip-Ratio

4.1 Control Goals

Coarse control of slip-ratio has been demonstrated by conventional ABS and TC systems. This chapter describes how much finer control can be achieved by leveraging the merits of an electric motor independently controlling the torque input to a wheel. In this respect, these merits are three-fold:

1. Electric motors can respond 10 times more quickly than electro-hydraulic brake systems [6], allowing for higher bandwidth slip-ratio control.
2. Electric motors can generate torque bi-directionally. This allows the same controller to be developed for the generation of both driving and braking slip-ratio.
3. Unlike electro-hydraulic brake and engine systems, the torque output by the electric motor can be estimated with high accuracy [6].

As will be demonstrated in this chapter, this final merit allows for the fast and accurate estimation of longitudinal tire force utilizing the Controller Output Observer (COO) concept [28]. This estimate can be used to inform high level controllers, as will be discussed in Chapter 5.

This chapter proposes a slip ratio controller which quickly and accurately achieves a desired slip ratio. The longitudinal tire force estimated by the COO is represented as a disturbance, and rejected by the control law. This control architecture is similar to the disturbance observer presented in [29] [30] [31] [32]. Indeed, the proposed control structure is shown to be equivalent to the disturbance observer structure under certain circumstances. However, the proposed control structure utilizing the COO can be realized without requiring plant inversion, and can be calibrated using classical feedback control techniques [12]. The result is a slip-ratio controller which robustly tracks desired slip-ratio, regardless of road surface and tire operating condition.

This chapter is organized as follows: A linear model of wheel and tire dynamics is presented followed by presentation of the Controller Output Observer as applied to predict longitudinal tire force. A disturbance observer is applied to the same problem, and its potential equivalence to the COO is presented. A proposed slip ratio controller utilizing the COO for disturbance rejection is proposed with some linear simulation results. Finally, the slip ratio controller is applied on an experimental vehicle and its performance is tested on varied road surfaces. The proposed control structure tracks desired slip ratio quickly and accurately while providing a useful estimate of generated longitudinal tire force.

4.2 Linear Model of Wheel Dynamics

A schematic of a modeled wheel is shown in Figure 4.2.1. The wheel has a moment of inertia J and a radius R. Torque τ can be applied to the wheel and longitudinal tire force F_x is generated at the contact patch between the tire and the road surface. The wheel rotates with angular velocity ω and moves with a longitudinal velocity at its center V_w. A summation of the moments about the axis of rotation of the wheel generates the dynamical equation

$$\dot{\omega}(t) = \frac{1}{J}\tau(t) - \frac{R}{J}F_x(t) \tag{4.2.1}$$

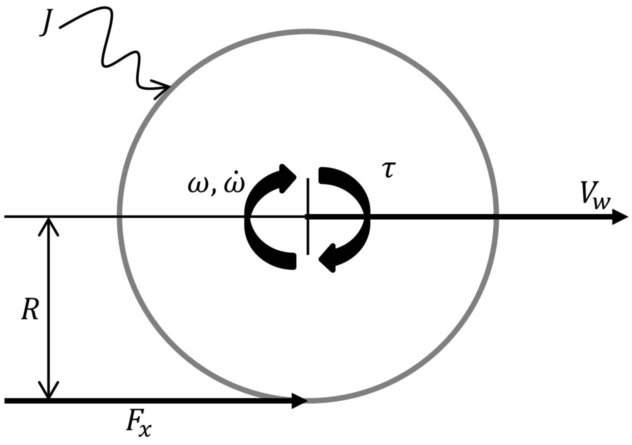

Figure 4.2.1: Wheel Schematic Diagram

To simplify analysis, only a single wheel will be studied connected to a mass m equivalent to a quarter of the vehicle's sprung mass. A summation of forces in the longitudinal direction renders the second dynamical equation

$$\dot{V}_w(t) = \frac{1}{m} F_x(t) \tag{4.2.2}$$

Together, Eqns. (4.2.1) and (4.2.2) describe the dynamics of a single wheel.

Longitudinal force F_x is generated at the contact patch between the tire and the road surface. The generation of this force is dependent on the longitudinal deformation of the tire, termed the slip-ratio

$$\sigma = \frac{R \cdot \omega - V_w}{\max \left(R \cdot \omega, V_w \right)} \tag{4.2.3}$$

as shown in Figure 4.2.2 for three hypothetical tires. The friction coefficients $\mu = 0.2, 0.5$ and 0.8 correspond to a tires operating on icy pavement, wet pavement and dry pavement respectively. As is evident in the figure, tires operating with relatively small slip-ratio generate longitudinal force in approximately linear proportion to slip-ratio with slope C_x. Assuming

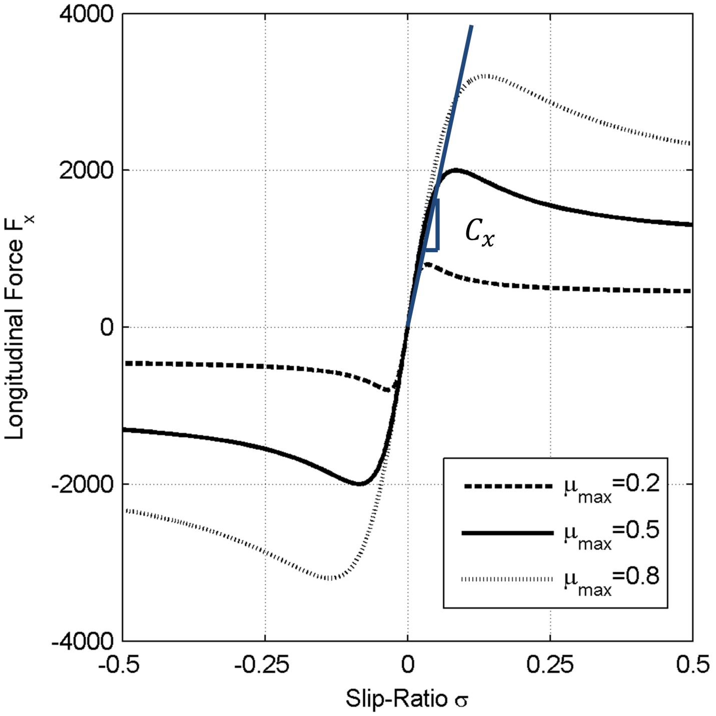

Figure 4.2.2: Linear Model of Longitudinal Tire Force Generation for Tires with Normal Loading $F_z = 4000N$

small slip-ratio, longitudinal tire force can be represented by

$$F_x \approx C_x \sigma \tag{4.2.4}$$

However, as slip ratio increases beyond this linear region the tire begins to progressively slip on the road surface and force generation saturates. This saturation occurs earlier for tires operating on lower friction surfaces. It is desirable that the slip-ratio controller developed in this work be robust to the non-linear region of tire operation which is frequently encountered during operation on slippery road surfaces.

Model Linearization

Slip-ratio, as presented in Eqn. (4.2.3), is a non-linear function of states ω and V_w. To simplify analysis, slip-ratio during braking will be represented as

$$\sigma = \frac{R \cdot \omega - V_w}{V_w} \tag{4.2.5}$$

with the complementary analysis for slip-ratio during acceleration omitted for brevity. A variable can be linearized by representation as an initial value plus a deviation about the initial value as

$$x = x_o + \Delta x \tag{4.2.6}$$

To facilitate linear analysis, the non-linear slip ratio described in Eqn. (4.2.5) is linearized as

$$\Delta\sigma = \frac{\partial\sigma}{\partial\omega}\Delta\omega + \frac{\partial\sigma}{\partial V_w}\Delta V_w = \frac{R}{V_{w_o}}\Delta\omega - \frac{R\omega_o}{V_{w_o}^2}\Delta V_w \tag{4.2.7}$$

where variables preceded with Δ represent linearized quantities and variables ω_o and V_{w_o} represent initial values for which the linearization centers. Augmenting Eqns. (4.2.1) and (4.2.2) with Eqns. (4.2.4) and (4.2.7), the linear system of equations describing the wheel dynamics with a linear tire model were developed as

$$\begin{bmatrix} \Delta\dot{\omega}(t) \\ \Delta\dot{V}_w(t) \end{bmatrix} = \begin{bmatrix} -\frac{R^2C_x}{JV_{w_o}} & \frac{R^2C_x\omega_o}{JV_{w_o}^2} \\ \frac{C_xR}{mV_{w_o}} & -\frac{C_xR\omega_o}{mV_{w_o}^2} \end{bmatrix} \begin{bmatrix} \Delta\omega(t) \\ \Delta V_w(t) \end{bmatrix} + \begin{bmatrix} \frac{1}{J} \\ 0 \end{bmatrix} \Delta\tau(t) \tag{4.2.8}$$

with output equation

$$\begin{bmatrix} \Delta\omega(t) \\ \Delta\sigma(t) \end{bmatrix} = \begin{bmatrix} 1 & 0 \\ 0 & 1 \end{bmatrix} \begin{bmatrix} \Delta\omega(t) \\ \Delta\sigma(t) \end{bmatrix} \tag{4.2.9}$$

Transforming this system of equations from the time domain to the Laplace domain and applying Cramer's rule to solve the system of equations with respect to a single output, the following transfer functions were developed

$$G_{\Delta\tau\to\Delta\omega}(s) = \frac{1}{J}\frac{s+C_n}{s(s+C_d)} \tag{4.2.10}$$

$$G_{\Delta\tau\to\Delta\sigma}(s) = \frac{R}{JV_{w_o}}\frac{1}{s+C_d} \tag{4.2.11}$$

where

$$C_n = \frac{C_x R\omega_o}{mV_{w_o}^2} \tag{4.2.12}$$

and

$$C_d = \frac{RC_x}{V_{w_o}}[\frac{R}{J} + \frac{\omega_o}{mV_{w_o}}] \tag{4.2.13}$$

The variable s represents the operator variable in the Laplace domain. $G_{\Delta\tau\to\Delta\omega}(s)$ provides the transfer function from torque input to wheel speed output, while $G_{\Delta\tau\to\Delta\sigma}(s)$ represents the transfer function from torque input to slip ratio output. Both transfer functions are stable assuming only positive entries forming the coefficients in Eqns. (4.2.12) and (4.2.13) which is guaranteed by limiting analysis to forward vehicle velocity. The remainder of this chapter will describe the development of a system to control the slip-ratio of this linearized system. However, the "Δ" notation will be omitted for readability.

4.3 Controller Output Observer

The relationships which govern the generation of tire forces are often complicated and cannot be measured directly. Instead, an observer termed the Controller Output Observer (COO) [28] is proposed to provide an estimate of longitudinal tire force $\hat{F}_x$ which will be used by the slip ratio controller proposed later in this chapter. A block diagram representation of the COO is provided in Figure 4.3.1.

The COO constructs a model of wheel dynamics as

$$\dot{\omega}_m(t) = \frac{1}{J}\tau(t) - \frac{R}{J}\hat{F}_x \tag{4.3.1}$$

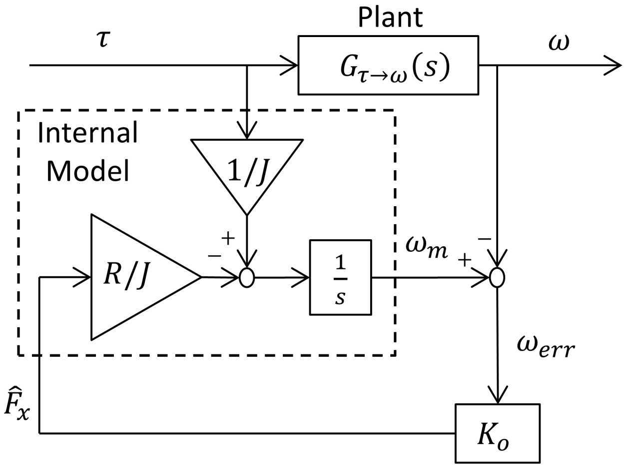

Figure 4.3.1: Controller Output Observer Block Diagram

with longitudinal tire force as an unknown input quantity and ω_m representing the COO modeled wheel speed. The modeled system and physical system are both subjected to the same known input wheel torque τ. It is a merit of electric motors that this input quantity can be known accurately [6]. The resulting measured and modeled wheels speeds ω and ω_m are then compared, generating the error term ω_{err}. This error is attributed to the unknown quantity $\hat{F}_x$, and input into the model of wheel dynamics after being multiplied by positive observer gain K_o. It is important to note that modeling error and disturbance input cannot be deciphered mathematically. Thus, error in model parameters R and J will be assumed as disturbance inputs, resulting in error in estimated longitudinal force $\hat{F}_x$. It therefore stands to reason that effort should be made to ensure that estimates of these parameters are reasonably accurate during vehicle operation.

Setting the input torque to zero, the transfer function from plant (measured) wheel speed ω to internally modeled wheel speed ω_m can be found as

$$\frac{\omega_m(s)}{\omega(s)} = \frac{\frac{R}{J}K_o}{s + \frac{R}{J}K_o} \tag{4.3.2}$$

which represents a stable first order system with prescribed positive observer gain K_o. This system can be alternatively represented in time-constant form as

$$G_{\omega \to \omega_m}(s) = \frac{1}{\tau s + 1} \tag{4.3.3}$$

where $\tau = \frac{J}{RK_o}$ is the system's time constant. In this form it is evident that increasing observer gain K_o results in reduced system time-constant, and thus quicker response. Additionally, the system's DC-gain, evaluated by prescribing the Laplacian operator to $s \to 0$, is unity. Thus, subjected to a step in measured wheel speed ω, the internally modeled wheel speed will exponentially approach the measured wheel speed with zero steady-state error. It is shown in [28] that if the modeled outputs converge toward the measured outputs, the quantities estimated by the COO will converge towards their true values. Thus the COO should provide an estimate of longitudinal tire force with zero steady state error. As the COO structure makes no assumption regarding tire model and instead treats tire forces as a disturbance, this convergence result should hold regardless of operating surface and level of tire saturation.

4.3.1 Linear COO Validation

The linear system described in Section 4.2 was simulated subjected to a pulse of brake torque, initiating at t=0.1 and terminating at t=0.3 seconds. In addition to implementing the continuous time COO developed in the previous section, a discrete variant was proposed by utilizing trapezoidal integration [33] to approximate the continuous time integrator. This discrete variant was implemented with a sampling frequency of $100Hz$, a reasonable value for modern vehicle motion control systems.

Figure 4.3.2 shows the physical and modeled wheel speeds in response to the input torque. Both the continuous and discretely modeled wheel speeds track the decreasing physical wheel speed with constant error, and the constant physical wheel speed with zero steady-state error. These observations are commensurate with a stable first order system with unity DC-gain.

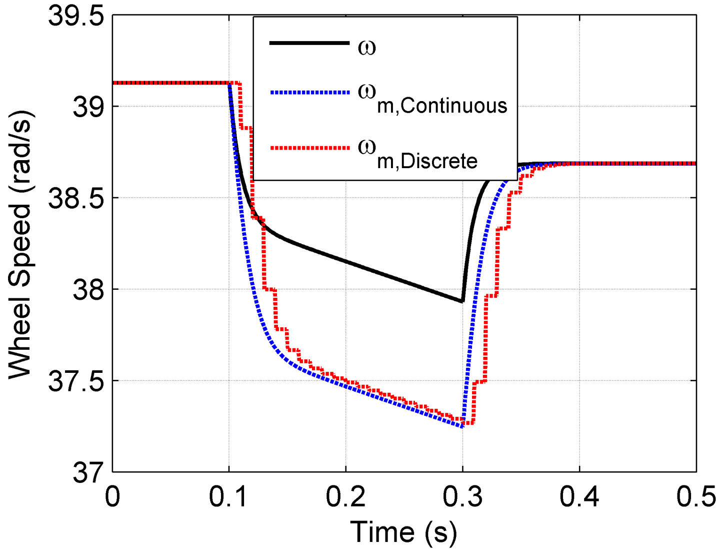

Figure 4.3.2: Measured Wheel-Speed Compared with Continuously and Discretely Modeled Wheel Speed During Pulse of Brake Torque, $K_o = 400$

Figure 4.3.3 shows the true longitudinal force and the longitudinal forces estimated by the continuous and discretely realized COO. It is interesting to note that even during periods of transient wheel-speed the COO is able to estimate longitudinal force with zero steady-state error. Additional analysis was necessary to explain this phenomenon.

Linear COO Error Dynamics

It is our goal to derive an analytical expression for longitudinal force estimation error $F_{x_{error}}$ as a function of wheel torque input τ where

$$F_{x_{error}} = F_x - \hat{F}_x \tag{4.3.4}$$

and the analytical expression for the *true* longitudinal force is

$$F_x = C_x \sigma = C_x G_{\tau \to \sigma}(s) \tau \tag{4.3.5}$$

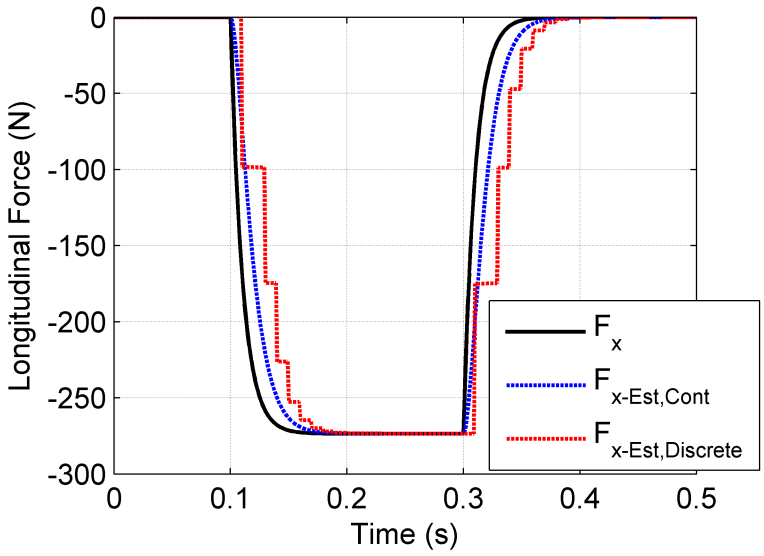

Figure 4.3.3: Actual and Continuously and Discretely Estimated Longitudinal Tire Force During Pulse of Brake Torque, $K_o = 400$

assuming the linear tire model of Eqn. (4.2.4). Therefore, in transfer function form

$$G_{\tau \to F_x}(s) = \frac{F_x}{\tau} = C_x G_{\tau \to \sigma}(s) \tag{4.3.6}$$

Referring back to Figure 4.3.1 it is possible to determine that the relationship between torque input and longitudinal force estimate for the COO is

$$G_{\tau \to \hat{F}_x}(s) = \frac{\hat{F}_x}{\tau} = K_o \frac{\frac{1}{J} - sG_{\tau \to \omega}(s)}{s + \frac{K_o R}{J}} \tag{4.3.7}$$

Subtracting these two transfer functions, we develop the following analytical expression for estimation error

$$G_{\tau \to F_{x_{error}}}(s) = \frac{F_{x_{error}}}{\tau} = G_{\tau \to F_x}(s) - G_{\tau \to \hat{F}_s}(s) = \frac{C_x R}{J V_{w_o}} \frac{s}{(s + C_d)(s + \frac{K_o R}{J})} \tag{4.3.8}$$

It is interesting to note that when decomposed via partial fraction expansion, this transfer function will result in two stable exponentially decaying terms in the time domain. One term's speed of decay is governed by C_d, and is thus a function of the physical system parameters, as shown in Eqn. (4.2.13). Therefore, the maximum speed of estimation error decay is a direct function of the system parameters. Therefore it is suggested that the observer gain be selected such that

$$K_o \leq C_d \frac{J}{R} \tag{4.3.9}$$

as larger values will not result in faster decay of estimation error.

It was the goal of this analysis to determine why the COO exhibited zero steady-state estimation error when subjected to a step in input torque, as presented in Figure 4.3.3. To this end, the final value theorem

$$y(\infty) = \lim_{t \to \infty} y(t) = \lim_{s \to 0} s y(s) \tag{4.3.10}$$

is applied to the equation of error dynamics when subjected to a step in input torque

$$F_{x_{error}}(s)|_{\tau = step} = G_{\tau \to F_{x_{error}}}(s) \frac{1}{s} \tag{4.3.11}$$

resulting in

$$F_{x_{error}}(\infty)|_{\tau = step} = \lim_{s \to 0} s \frac{C_x R}{J V_{w_o}} \frac{s}{(s + C_d)(s + \frac{K_o R}{J})} \frac{1}{s} = 0 \tag{4.3.12}$$

As is evident in Eqn. (4.3.12), the COO should exhibit zero steady-state estimation error when subjected to a step in input torque τ.

4.3.2 Equivalence to Disturbance Observer

Another approach proposed for estimating unknown inputs is the disturbance observer [29] [30]. Treating the last term of the wheel dynamic model shown in Eqn. (4.2.1) as an unknown disturbance, the nominal transfer function from input wheel torque to resulting wheel speed is

$$G^n_{\tau \to \omega}(s) = \frac{1}{J} \frac{1}{s} \tag{4.3.13}$$

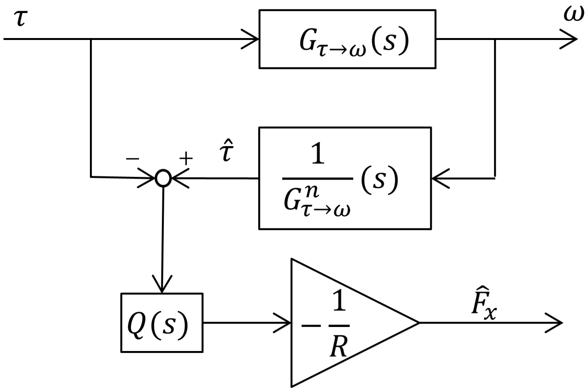

Figure 4.3.4: Disturbance Observer Block Diagram

The disturbance observer takes the measured output from the physical system and passes it through the inverted nominal plant model, as shown in Figure 4.3.4. The output from the inverted plant model, $\hat{\tau}$, is then compared with the known input torque, τ. The difference between the two signals is the result of unknown disturbances as well as discrepancies between the nominal plant model and the physical plant. The low pass filter $Q(s)$ is applied to make the inverted plant model realizable, as well as to smooth the disturbance estimate.

It can be shown that the disturbance observer shown in Figure 4.3.4 can be made equivalent to the controller output observer shown in Figure 4.3.1 by selecting a low pass filter of the form

$$Q(s) \triangleq \frac{\frac{RK_o}{J}}{s + \frac{RK_o}{J}} \tag{4.3.14}$$

The disturbance observer is a mature concept, used in many applications [31]. Its main objective is to reject unknown disturbances and modeling uncertainties, thus improving the robustness of the controlled system. However, the classical disturbance observer requires inversion of the nominal plant transfer function. If this transfer function has non-minimum phase (unstable) zeros, its inverse will have unstable poles and be unsuitable for application. Non-minimum phase zeros are common in discrete representations of systems as a result of sampling. Indeed, a bilinear approximation [33]

$$s \approx \frac{2}{T_s}\frac{z-1}{z+1} \tag{4.3.15}$$

where T_s represents the discrete sampling time, and z is the operator variable in the discrete domain, can be used to transform the nominal plant transfer function shown in Eqn. (4.3.13) to the discrete transfer function

$$G^n_{\tau\to\omega}(z^{-1}) = \frac{T_s}{2J}\frac{1+z^{-1}}{1-z^{-1}} \tag{4.3.16}$$

It is necessary to utilize the inverse of this transfer function for disturbance observer implementation as

$$\frac{1}{G^n_{\tau\to\omega}(z^{-1})} = \frac{2J}{T_s}\frac{1-z^{-1}}{1+z^{-1}} \tag{4.3.17}$$

which has a pole located at $z = -1$ which describes undamped oscillatory behavior (chattering) and is undesirable.

Tomizuka [34] proposes the zero phase error tracking method of approximating the inverse of a discrete plant with non-minimum phase zeros. This method has been proven for motion control applications [32]. However, the COO method of disturbance estimation provides an alternative which does not require the inversion, or approximate inversion of the nominal plant. For this reason, the COO structure will be used for disturbance estimation for the remainder of this work.

4.4 Slip-Ratio Control with Disturbance Rejection

As was shown in Figure 4.2.2, tire slip ratio is strongly correlated with longitudinal force generation. Additionally, by avoiding regions of excessive slip ratio, tire performance can be optimized. For these reasons it is desirable to implement a slip ratio controller at each electrically driven wheel. Eqn. (4.2.1) shows that wheel dynamics are governed by the torque input from the electric motor, as well as the longitudinal force developed by the tire. Tire force generation, although correlated with slip ratio, also depends on tire slip angle and immeasurable factors such as road surface and tire condition [10]. The proposed slip ratio controller treats the longitudinal tire force as an unknown disturbance. This disturbance is estimated using a COO and explicitly rejected by the control law. This architecture provides quick and accurate slip ratio control which is robust to changes in immeasurable factors such as road surface and tire condition.

The following control law is proposed

$$\tau(t) = u(t) + R\hat{F}_x(t) \tag{4.4.1}$$

which adds the estimated disturbance $R\hat{F}_x(t)$ to the output of a slip-ratio feedback controller $u(t)$. When applied to the model of wheel dynamics shown in Eqn. (4.2.1), the proposed control law reduces wheel dynamics to

$$\dot{\omega}(t) = \frac{1}{J}[u(t) - R(F_x(t) - \hat{F}_x(t))] \tag{4.4.2}$$

From this equation it is evident that as the estimated longitudinal force approaches the actual longitudinal force the equation of wheel dynamics is reduced to approximately

$$\dot{\omega}(t) \approx \frac{1}{J}u(t) \tag{4.4.3}$$

Thus, as the COO estimate of longitudinal force converges toward the true value, as is guaranteed in [28], the model of wheel dynamics converges towards the straight-forward control of a rotary inertia. This is a desirable result as the proposed control structure is not disturbed by changing road surface or tire condition.

A block diagram of the proposed slip ratio controller utilizing a COO for disturbance rejection is shown in Figure 4.4.1. K_o is the observer gain and $G_c(s)$ represents the slip ratio

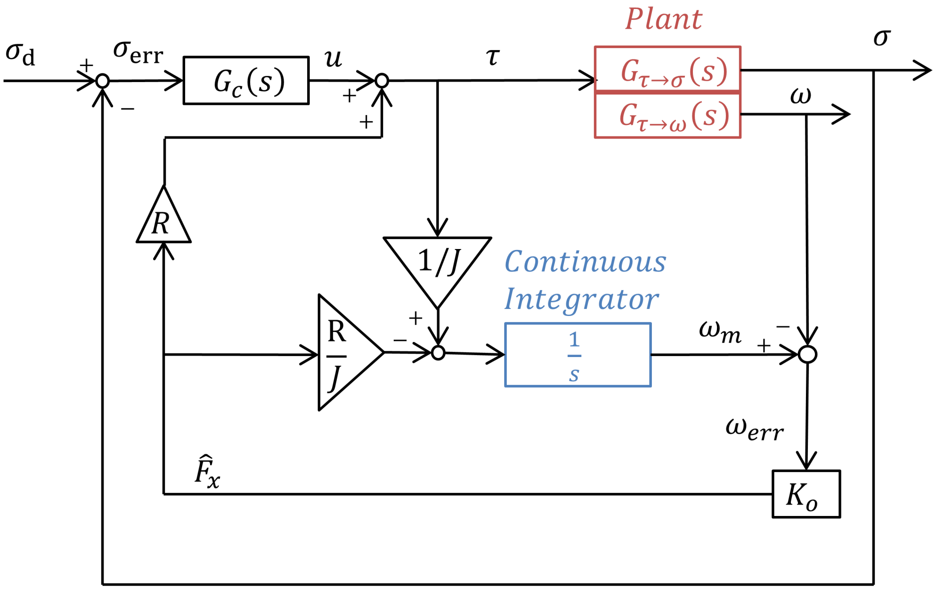

Figure 4.4.1: Continuous Slip Ratio Control with COO Disturbance Rejection Block Diagram

feedback controller, and has been implemented as the Proportional-Integral (PI) controller

$$G_c(s) = K_p + \frac{1}{s}K_i \tag{4.4.4}$$

where K_p and K_i are tunable gains. Although a PI controller is presented in this work, any controller which is capable of driving an error towards zero can be considered.

4.4.1 Discrete Realization

The slip-ratio controller proposed in Figure 4.4.1 requires knowledge of current wheel-speed in order to estimate current longitudinal force, and determine the required control response. However, a digitally implemented system requires that the wheel-speed be measured at discrete sampling intervals. This sampling process can be modeled by a Zero-Order-Holds (ZOH) as shown in Figure 4.4.2. In this situation, it is necessary to delay the torque input to the COO as well as longitudinal force estimate by one sampling period z^{-1} to ensure that

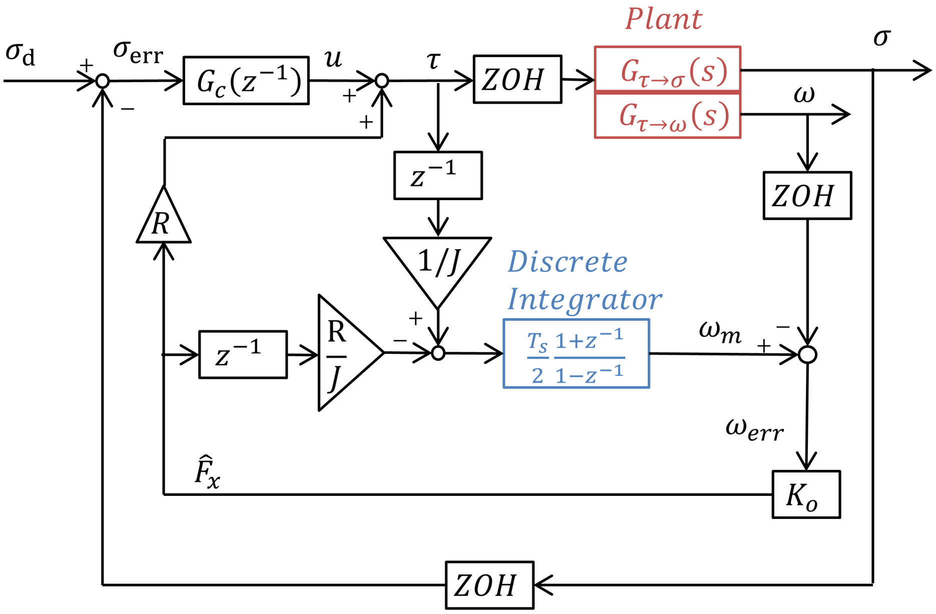

Figure 4.4.2: Discrete Slip Ratio Control with COO Disturbance Rejection

they correspond with the sampled wheel-speed measurement. Additionally, the continuous time integrator utilized by the COO is replaced by a discrete approximation utilizing a bilinear transformation. Finally, the continuous PI controller is replaced by the discretely implementable approximation

$$G_c(z^{-1}) = K_p(1 - z^{-1}) + \frac{T_s}{2}K_i(1 + z^{-1}) \tag{4.4.5}$$

again utilizing the bilinear transformation.

The discrete slip-ratio controller can be implemented with the following recursive steps:

1. Utilize measured wheel-speed $\omega(k)$ as well as previously estimated longitudinal force $\hat{F}_x(k-1)$ and previously actuated wheel torque $\tau(k-1)$ to estimate current longitudinal force $\hat{F}_x(k)$

2. Evaluate discrete slip-ratio feedback controller $G_c(z^{-1})$ to determine control effort $u(k)$

3. Actuate control torque $\tau(k) = u(k) + R\hat{F}_x(k)$

where $k-1$ and k represent discrete samples of continuous signals separated by one control iteration , i.e. $T_s = t(k) - t(k-1)$.

4.4.2 Linear Slip-Ratio Controller Validation

The response of the discretely realized slip ratio controller to a step in desired slip-ratio was simulated with and without disturbance rejection from the COO. Figure 4.4.3 shows the response of these two systems with controllers operating with sampling time $T_s = 100Hz$. The PI gains K_p and K_i were selected such that the system with COO disturbance rejection exhibited minimal oscillations and overshoot. The same gains were then used in a system using only a PI controller to highlight the effect of adding the COO disturbance rejection. As is evident from the figure, the use of COO disturbance rejection vastly improved the settling time of the discrete control system. The discrete controller without disturbance rejection performed poorly, requiring significantly larger gains to reduce settling time. This necessary increase in gain can result in an increasingly oscillatory response for the system without COO disturbance rejection. If higher bandwidth slip-ratio tracking is required it is suggested that a feedforward control element be added.

In addition to improving slip ratio response, use of the COO for disturbance rejection also provides a near real time estimate of longitudinal tire force $\hat{F}_x$. Figure 4.4.4 shows the estimated and actual tire forces for the discretely realized controller with COO disturbance rejection. As is evident from the figure, the COO quickly and accurately estimated longitudinal tire force. A similar validation carried our with a nonlinear plant can be found in [12].

4.5 Experimental Validation

The conventional powertrain of a B-class production vehicle was replaced with two wheel-motors independently driving both rear wheels of an experimental vehicle. The vehicle is

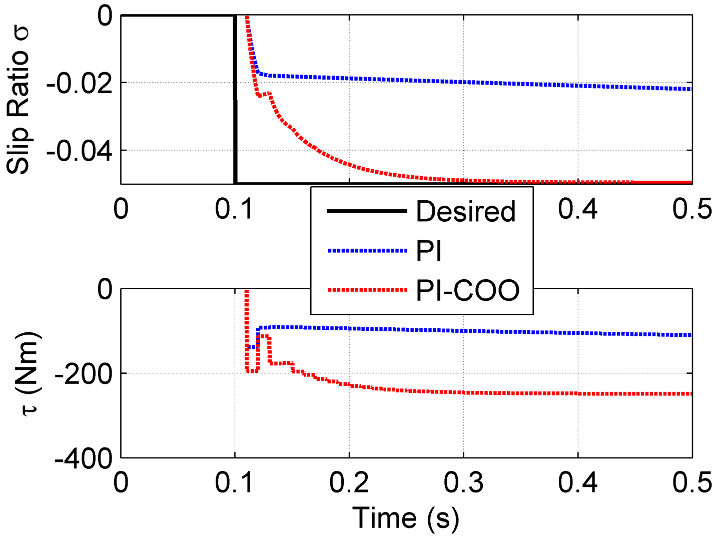

Figure 4.4.3: Step Response of Discrete Slip Ratio Controllers with and without Disturbance Rejection

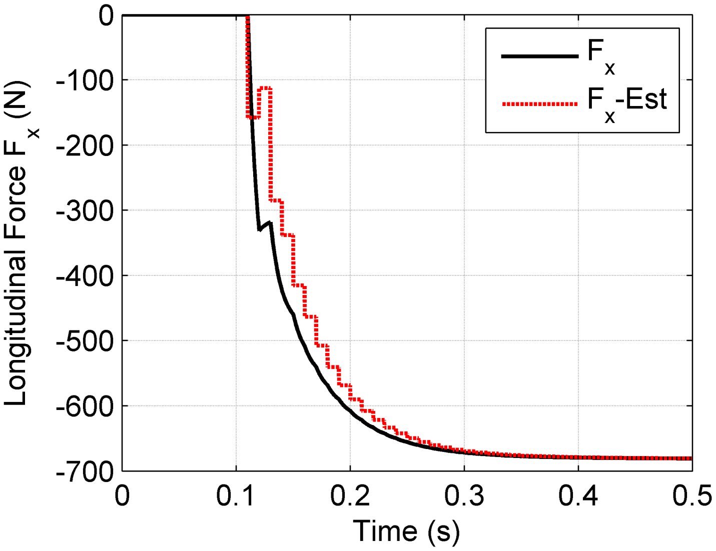

Figure 4.4.4: Estimated and Actual Longitudinal Forces

shown in Figure 4.5.1 being launched on a split-μ surface for controller validation. The left tires of the vehicle are on pavement, while the right tires of the vehicle are on a very low friction surface.

The complete control architecture presented in Chapter 2 was applied to the vehicle for

Figure 4.5.1: Experimental Vehicle with Wheel-Motors Installed at Each Rear Wheel, Being Tested on a Slip-μ Surface

control validation, operating at a discrete sample frequency of approximately $60Hz$. The performance of the slip-ratio controller during full throttle launch on the split-μ surface is presented in Figure 4.5.2. The control allocation functionality discussed in Chapter 5 was employed, resulting in the non-symmetric desired slip-ratio commands, however they are similar enough to allow for comparison of the slip-ratio controller's performance on differing road surfaces.

The PI controllers discussed in Section 4.4 were implemented as only Proportional (P) controllers to simplify experimental calibration. However, even without integral control the desired slip-ratio is approximately achieved at both wheels. This is a particularly impressive feat when studying the right-rear tire which was operating on the low-μ surface. Indeed, it can be seen in Figure 4.5.3 that the right-rear tires is operating at and above the region of maximum force generation for a low-μ surface. Operating in this difficult region resulted in the slightly oscillatory behavior noted in Figure 4.5.2.

Figure 4.5.4 presents the torque requests made by the slip-ratio controllers of the left and right rear tires. As is evident from the figure, both controllers quickly increased torque requests in an attempt to achieve the desired slip-ratio. However, the variable operating

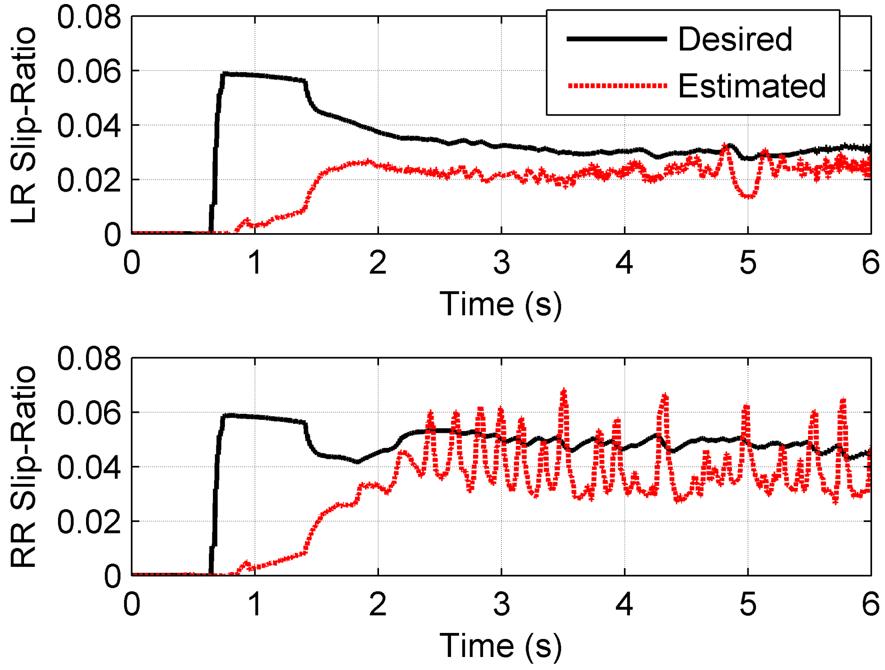

Figure 4.5.2: Desired and Estimated Slip-Ratios for Left and Right Rear Tires when Launched from a Stop with Left-Rear Tire on High-μ Surface and Right-Rear Tires on Low-μ Surface

surface between the two tires is quickly evident by $t = 2s$ where the torque request made of the right-rear wheel is quickly reduced. It is suggested that feedforward control functionality should be employed in future renditions of this slip-ratio controller to further reduce settling time.

Figure 4.5.5 presents the estimated longitudinal force for the right-rear tire. In addition to the estimate made by the COO, an estimate is obtained neglecting wheel dynamics and assuming the tire is rigidly fastened to the road surface with the relationship

$$\hat{F}_x = \frac{\tau}{R} \tag{4.5.1}$$

The purpose of this presentation is to sanity check the estimates made by the COO. As

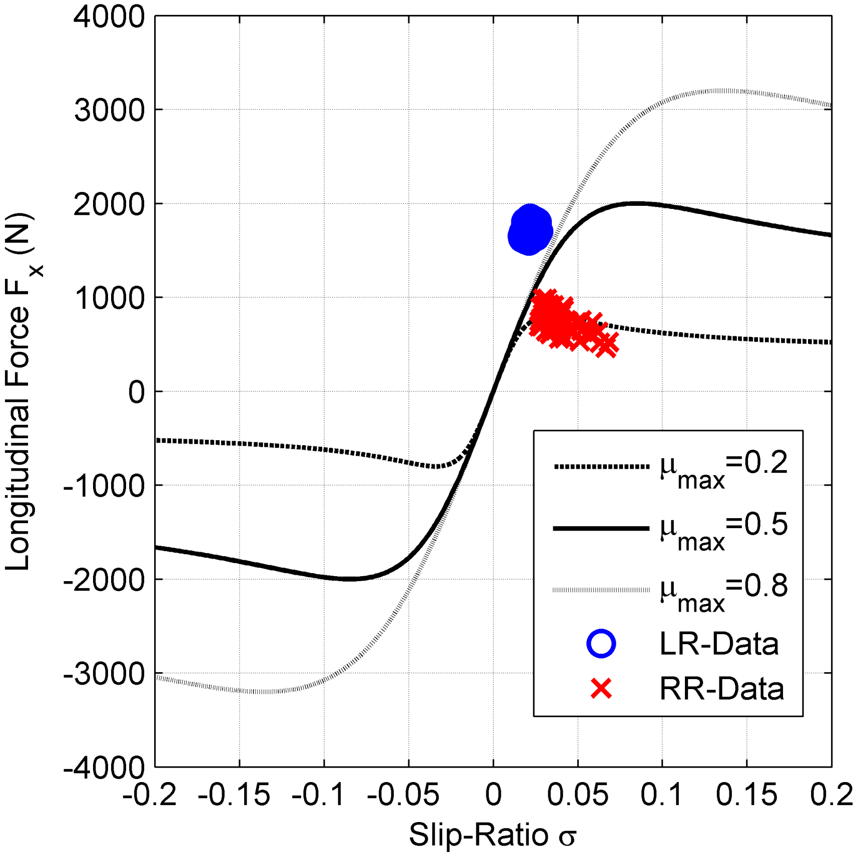

Figure 4.5.3: Longitudinal Force vs. Slip-Ratio for Tires Operating on Varied Road Surfaces, Generated using Pacejka MF [10] with Experimental Data Points Superimposed

is evident from the figure, the COO estimate is generally slightly delayed from the non-dynamical estimate. This delay is reasonable, as the COO accounts for the inertia of the wheel. Additionally, tire deformation is of itself a dynamic quantity, requiring finite time for force to be generated in response to torque input. In addition to delayed response, the COO estimate of longitudinal force is also generally of smaller magnitude compared with the non-dynamic estimate. This discrepancy can be explained by the rolling resistance, bearing resistance and tire rolling radius uncertainty which are accounted for by the COO, but not by the non-dynamic model. In general, the COO estimate of longitudinal force is deemed accurate, and is relied upon for higher-level control system functionality discussed in Chapter 5.

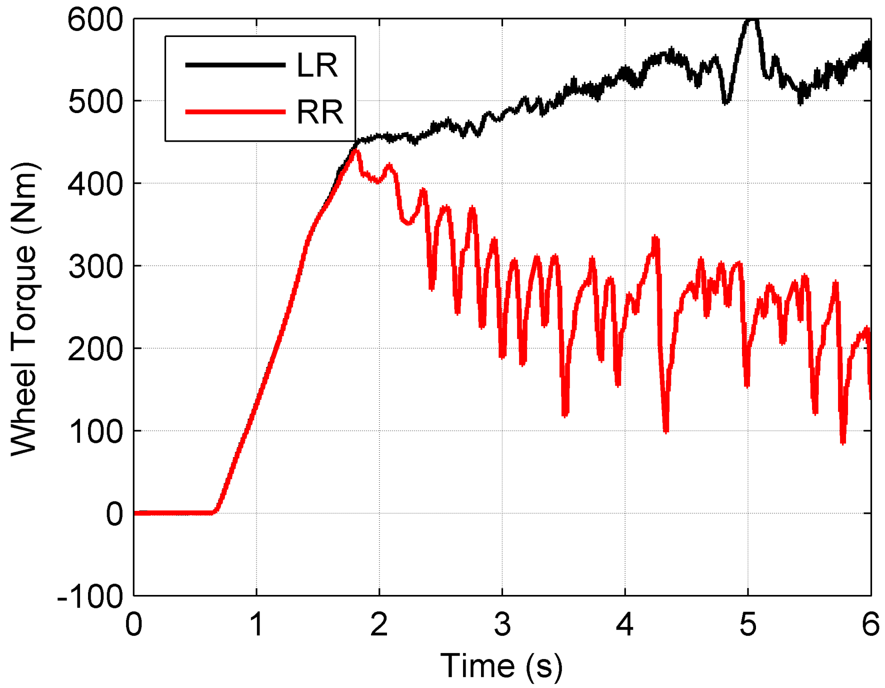

Figure 4.5.4: Requested Wheel Torques from Slip-Ratio Controller

4.6 Summary of Slip-Ratio Controller

In this chapter a slip-ratio controller has been proposed to take advantage of the merits of the wheel-motored vehicle. The controller is similar in form to the classical disturbance observer. However, the Controller Output Observer (COO) is proposed for disturbance estimation to avert the need for nominal plant inversion. The result is a practically implementable slip-ratio controller which is robust to changing road surface and tire condition. Additionally, as a byproduct of the controller's structure, a fast and accurate estimate of longitudinal tire force is obtained. This estimate is useful in determining tire saturation and informing higher-level control decisions. The proposed slip-ratio controller is validated through linear system simulation, as well as experimental testing on a wheel-motored vehicle.

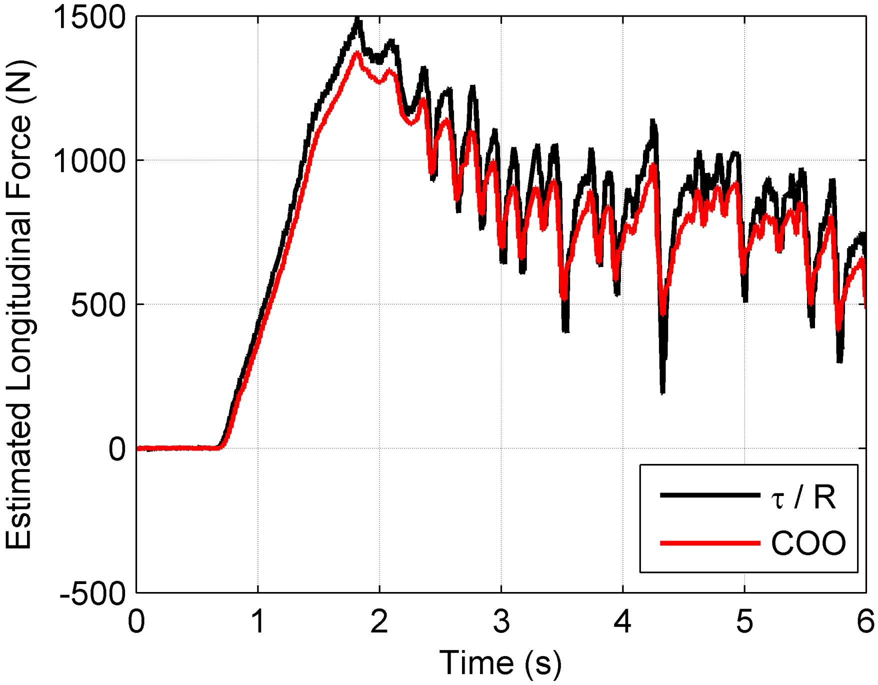

Figure 4.5.5: Estimated Longitudinal Force Generated by Right-Rear Tire

Chapter 5

Allocation of Slip-Ratio

5.1 Control Allocation

As the wheel motored vehicle is generally over actuated, i.e. it has more actuators than control goals, a control allocation framework is proposed [35]. This framework separates the large problem of controlling planar vehicle dynamics into three tractable sub-problems: high-level control, control allocation and low-level control. The interested reader may wish to revisit Section 2.2 for a thorough introduction to the proposed system architecture.

This chapter focuses on the development of the control allocation problem. Its task is to generate targets for the low-level controllers such that the generalized virtual forces requested by the high-level controller are achieved optimally, or at worst sub-optimally. Three control allocation problems are developed in this work. The first utilizes in depth knowledge of the constitutive relations by which tires generate force. This controller is not practical, but is developed to provide a benchmark for assessing the performance of the intended sub-optimal result – since it represents the limit of physically achievable performance. A suboptimal variant of this control allocation problem is then developed by incorporating simplifying assumptions. Unfortunately, these assumptions result in the loss of important tire saturation information and thus a decrease in system performance. Finally, a variant of the realizable controller is proposed which utilizes a fuzzy inference system to regain some understanding of the tires' level of saturation.

Desired control effort is allocated to each corner of the vehicle via control allocation. It is the task of the low-level controllers to attempt to achieve the desired control effort by modulating independent wheel motor torque. In addition, the low-level controller can be augmented with the task of estimating valuable information relevant to tire saturation to help improve control allocation performance. Such a low-level controller is proposed in Chapter 4.

A simulation study is conducted to compare the performance of the three allocation controllers when implemented on a vehicle in the CarSim© simulation environment. It is shown that the performance of the sub-optimal control allocation problem with fuzzy adaptation approaches the benchmark performance of the optimal control allocation problem. Experimental validation is then conducted on a B-class production vehicle with conventional powertrain replaced by two wheel-motors installed at the rear wheels. It is shown that the control allocation framework allows for the intuitive calibration of planar vehicle dynamics. Additionally, it is shown that the fuzzy adaptation mechanism prevents tire saturation, resulting in near optimal performance, regardless of road surface.

5.2 Model of Tire Force Generation

Aside from aerodynamic drag, tires are the only method of imparting lateral and longitudinal forces on the vehicle. Under normal operation they act like a spring, generating force in proportion to deflection. However, the force generating capacity of a tire is limited by its normal loading and the coefficient of friction between the tire and the road surface. If this force generating capacity is exceeded, the tire will begin to progressively slip on the road surface, resulting in a saturation of force generation. This section will focus on the relationship between longitudinal slip-ratio, σ, and longitudinal/lateral tire force generation

F_x and F_y.

The longitudinal deflection of a tire is measured by slip ratio as shown in Eqn. (5.2.1) where V_w represents the velocity of the wheel center in the direction of wheel orientation. R represents the radius of the tire and ω its angular velocity. Slip-ratio describes the disparity between tire velocity and wheel velocity, normalized by the maximum of the two. Figure 5.2.1 shows longitudinal force generation with respect to slip-ratio for a road with varying coefficients of friction. Coefficients of friction ($\mu_{max} = \{0.2, 0.5, 0.8\}$) approximately represent icy pavement, wet pavement and dry pavement respectively. For small slip-ratios the relationship with force generation is approximately linear. However, as slip-ratio increases beyond the linear region the tire begins to progressively slide on the road surface, and force generation saturates.

$$\sigma = \frac{R \cdot \omega - V_w}{\max(V_w, R \cdot \omega)} \tag{5.2.1}$$

Figure 5.2.1 as well as Figure 5.2.2 to be described later were generated using the Pacejka Magic Tire Formula [10]. The Magic Formula (MF) relies upon semi-empirical functions of the form

$$F_{x,y} = D_{x,y} \sin\left[C_{x,y} \arctan B_{x,y}\sigma - E(B_{x,y}\sigma - \arctan B_{x,y}\sigma)\right] \tag{5.2.2}$$

to predict the force generation of a tire based upon its operating conditions. The parameters B_x, C_x, D_x, E_x are shaping coefficients for the longitudinal force generation function. These parameters are selected to fit the MF equations to data generated via experimental tire testing.

Similarly, lateral force generation with respect to slip ratio can be predicted with the selection of parameters B_y, C_y, D_y, E_y. Figure 5.2.2 shows the resulting curves for selected slip-angles of $\alpha = \{2^o, 4^o, 8^o\}$. Much like slip-ratio characterizes longitudinal tire deflection, slip-angle characterizes lateral tire deflection as

$$\alpha = -\arctan \frac{V_{w_\perp}}{|V_w|} \tag{5.2.3}$$

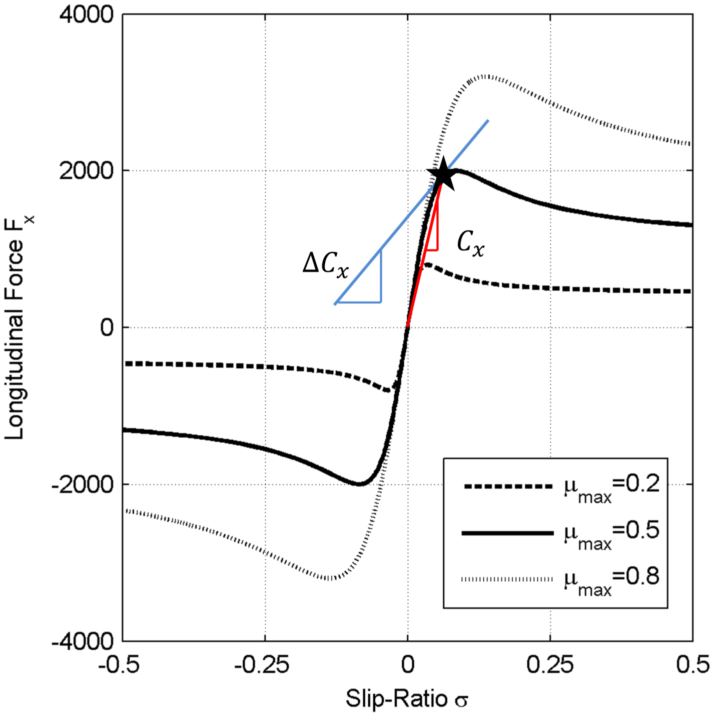

Figure 5.2.1: Constitutive Relationship Between Slip-Ratio and Longitudinal Force Generation for Surfaces with Varying Coefficient of Friction

where $V_{w_\perp}$ is the tire velocity perpendicular to the direction of wheel orientation. When $\sigma = 0$ the tire is said to be operating with pure side-slip, and generates its maximum lateral force. However, as slip-ratio increases, lateral force generation is decreased. This behavior can be explained by looking at the resultant force generated by the tire, F_R, defined by

$$F_R^2 = F_x^2 + F_y^2 \leq (\mu \cdot F_z)^2 \tag{5.2.4}$$

We expect that the resultant force generated by the tire should be less than or equal to the tractive capacity of the tire, $\mu \cdot F_z$, where F_z represents the tire's normal loading. As we increase slip-ratio, we observe an increase in longitudinal force generation, as depicted in Figure 5.2.1. Therefore, to obey our intuition regarding maximum resultant force, we require a decrease in lateral force generation with respect to slip-ratio, as is evident in

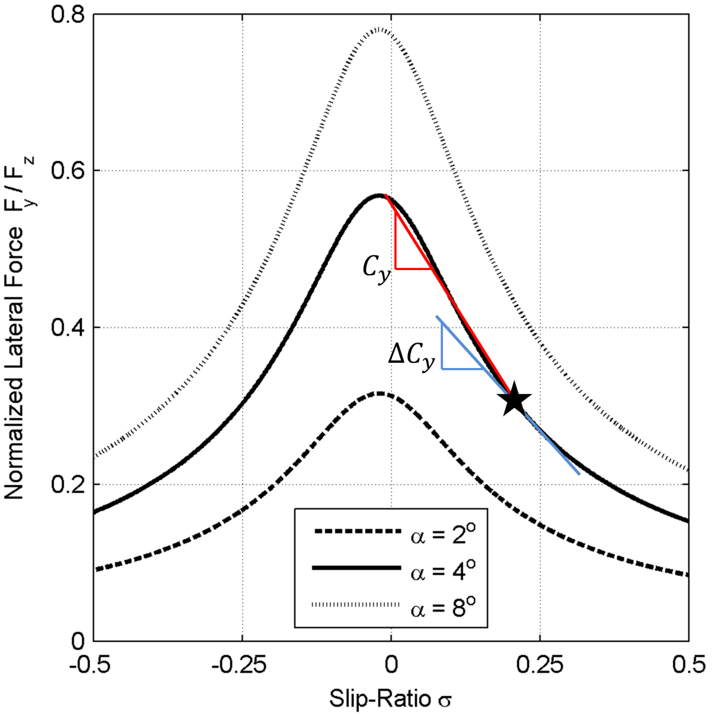

Figure 5.2.2: Constitutive Relationship Between Slip-Ratio and Lateral Force Generation for Tires Operating at Varying Slip-Angle

Figure 5.2.2. The coupling between longitudinal and lateral force generation with respect to slip-ratio should be accounted for during the intervention of a stability control system. The development of such a controller is a central focus of this chapter.

Concluding our discussion of tires and their force generating constitutive behavior we now introduce some definitions which will be used in the following sections. First, we introduce the longitudinal stiffness,

$$C_x = \frac{F_x}{\sigma} \tag{5.2.5}$$

as depicted in Figure 5.2.1. The longitudinal stiffness provides a linear representation of how the tire generates longitudinal force with respect to slip-ratio. Additionally we introduce the lateral stiffness,

$$C_y = \frac{F_y - F_{y_o}}{\sigma} \tag{5.2.6}$$

as depicted in Figure 5.2.2 where F_{y_o} represents the lateral force that the tire would have generated in pure side-slip ($\sigma = 0$). Thus, the lateral stiffness provides a linear representation of how lateral tire force diminishes with respect to slip-ratio. In addition to these linear descriptors, we introduce affine slopes as described by,

$$\Delta C_x = \frac{\partial F_x}{\partial \sigma} \tag{5.2.7}$$

$$\Delta C_y = \frac{\partial F_y}{\partial \sigma} \tag{5.2.8}$$

and depicted in Figures 5.2.1 and 5.2.2. The affine slopes can be calculated by differentiating Eqn. (5.2.2) with respect to slip-ratio, and evaluating the result at the current operating point. This derivative is generally unknown because the parameter of the MF cannot be determined online. The affine slopes are intended to be used only for the benchmark optimal control allocation problem.

It has been shown in Chapter 4 that F_x can be estimated quickly and accurately for vehicles utilizing independent electric motors for propulsion and braking. Additionally, a practical estimator of slip-ratio σ was proposed in Chapter 3. With this information, we can introduce an estimate of longitudinal stiffness as defined by

$$\hat{C}_x = \frac{\hat{F}_x}{\hat{\sigma}} \tag{5.2.9}$$

Conversely, it is much more difficult to generate an estimate of lateral stiffness, C_y. To do so would not only require an estimate of lateral force F_y, but also an estimate of the pure side-slip lateral force F_{yo}. Additionally, it is possible to generate estimates of ΔC_x as described in [36], but the quality of the estimate is dramatically effected by lack of persistence of excitation. Compounding the difficulties of estimating C_y with those of estimating ΔC_x, an accurate estimate of ΔC_y is deemed infeasible. It is a central focus of the following work to develop a realizable controller which utilizes only the readily available estimate of longitudinal stiffness $\hat{C}_x$ to make decisions regarding allocation. It will be shown that the performance of this controller can approach the performance of the benchmark optimal controller which utilizes $C_x, \Delta C_x, C_y, \Delta C_y$ within its routine.

5.3 The Control Allocation Problem

The control allocation portion of the system is tasked with proposing slip-ratios which best achieve the generalized virtual forces desired by the reference tracking controller. This problem will be developed assuming wheel-motors are installed at all four corners of the vehicle, but can be easily reduced for two-wheel implementation. The desired slip-ratios form the control effector vector

$$u^T = [\sigma_{lr}, \sigma_{rf}, \sigma_{lr}, \sigma_{rr}] \tag{5.3.1}$$

and the generalized virtual forces form the virtual force vector

$$v^T = [\Sigma F_x, \Sigma M_y, \Sigma F_y] \tag{5.3.2}$$

The term *generalized* is used to imply that not all terms are strictly in the force domain. For example, the sum of moments, ΣM_y, is in the torque domain. Additionally, the term *virtual* is used as no actuator exists to directly impart these generalized forces on the vehicle. Instead, they are a function of the forces generated by the tires at each corner of the vehicle. Figure 5.3.1 shows a free body diagram of the planar vehicle. The generalized virtual forces can be formulated as a sum of tire forces in the longitudinal direction V_x, as

$$\Sigma F_x = F_{x_{lf}} \cos\delta - F_{y_{lf}} \sin\delta + F_{x_{rf}} \cos\delta - F_{y_{rf}} \sin\delta + F_{x_{lr}} + F_{x_{rr}} \tag{5.3.3}$$

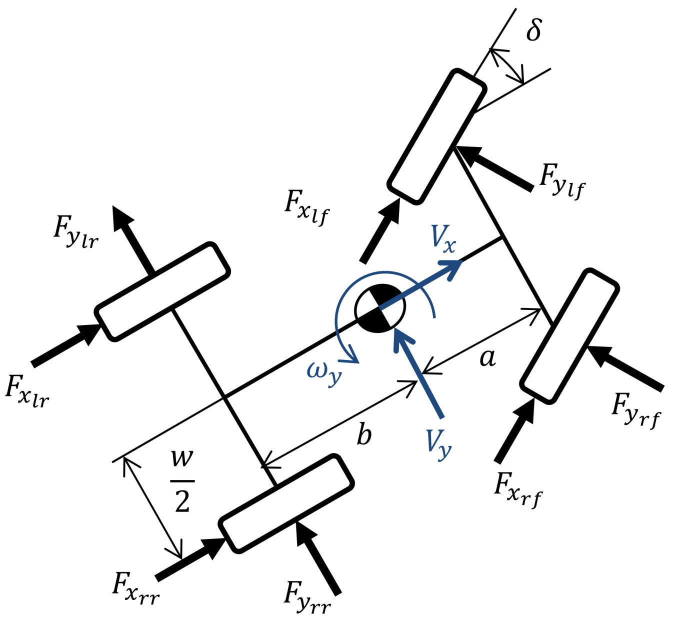

Figure 5.3.1: Free Body Diagram of Planar Vehicle

sum of moments about the center of gravity in the yaw direction ω_y as

$$\begin{aligned}\Sigma M_y = -\frac{w}{2}(F_{x_{lf}}\cos\delta - F_{y_{lf}}\sin\delta) + a(F_{y_{lf}}\cos\delta + F_{x_{lf}}\sin\delta)\\ \frac{w}{2}(F_{x_{rf}}\cos\delta - F_{y_{rf}}\sin\delta) + a(F_{y_{rf}}\cos\delta + F_{x_{rf}}\sin\delta)\\ -\frac{w}{2}F_{x_{lr}} - bF_{y_{lr}} + \frac{w}{2}F_{x_{rr}} - bF_{y_{rr}}\end{aligned} \quad (5.3.4)$$

and sum of tire forces in the lateral direction V_y as

$$\Sigma F_y = F_{y_{lf}}\cos\delta + F_{x_{lf}}\sin\delta + F_{y_{rf}}\cos\delta + F_{x_{rf}}\sin\delta + F_{y_{lr}} + F_{y_{rr}} \quad (5.3.5)$$

The variable δ represents the steered angle of the front wheels, and distance parameters a, b and $\frac{w}{2}$ locate the vehicles center of gravity.

The wheel motored vehicle is generally over actuated, i.e. it has more actuators than control goals (size(v) <size(u)). The result is that the desired generalized virtual forces can be achieved by infinitely many selections of the control effector vector u. A control allocation

technique is proposed to take advantage of this over actuation, achieving the desired virtual forces while imposing secondary objectives to allow for the selection of a unique solution which minimizes tire saturation. Control allocation has been widely used in aerospace and marine time industries, and is gaining prevalence in the automotive industry [35].

Although non-linear methods have been proposed, this work will focus on the assumption that a linear relationship exists between control effectors u and virtual forces v. This assumption simplifies computational burden and guarantees the existence of a globally minimal solution. The forces depicted in Figure 5.3.1 are generated by the tires at each corner of the vehicle, and are a non-linear function of slip-ratio, slip-angle and many other factors. Thus, to develop a linear relationship between u and v the tire must be linearized about its current operating state. An affine representation utilizing tire information $C_x, \Delta C_x, C_y, \Delta C_y$ as well as a linear representation utilizing only $\hat{C}_x$ will be presented.

5.3.1 Optimal Control Allocation

The first control allocation formulation to be discussed utilizes the following affine approximation of tire forces

$$F_{x_{ij}} \approx C_{x_{ij}} \sigma_{ij} + \Delta C_{x_{ij}} \Delta \sigma_{ij} \tag{5.3.6}$$

$$F_{y_{ij}} \approx C_{y_{ij}} \sigma_{ij} + \Delta C_{y_{ij}} \Delta \sigma_{ij} \tag{5.3.7}$$

where subscripts $ij = \{lf, rf, lr, rr\}$ represent each individual wheel. It is important to note that the variable F_y represents degradation in lateral force generation compared with pure side-slip as a result of change in slip-ratio, and not its absolute value. As the parameters utilized in this approximation could not be known in practice, the optimal control allocation problem is developed to benchmark the performance that the suboptimal control allocation problems developed in subsequent sections should approach. Utilizing the affine approximation of tire force generation, the generalized virtual forces can be regarded as the addition of two linear functions

$$v = B_o u_o + B_\Delta \Delta u \tag{5.3.8}$$

where

$$u = u_o + \Delta u \tag{5.3.9}$$

and

$$v = v_o + \Delta v \tag{5.3.10}$$

The notation u_o, v_o represents the current value of each vector, for which linearization is centered. The notation $\Delta u, \Delta v$ represents small changes in each vector about the linearized value. Combining Eqns. (5.3.3) and (5.3.5) with Eqns. (5.3.6) and (5.3.7) the linear control effectiveness matrix B_o can be constructed as

$$B_o = \begin{bmatrix} C^*_{x_{lf}} & C^*_{x_{rf}} & C_{x_{lr}} & C_{x_{rr}} \\ B_{o,21} & B_{o,22} & B_{o,23} & B_{o,24} \\ C^*_{y_{lr}} & C^*_{y_{rf}} & C_{y_{lr}} & C_{y_{rr}} \end{bmatrix} \tag{5.3.11}$$

where

$$\begin{aligned} C^*_{x_{lf}} &= C_{x_{lf}} cos(\delta) - C_{y_{lf}} sin(\delta) \\ C^*_{x_{rf}} &= C_{x_{rf}} cos(\delta) - C_{y_{rf}} sin(\delta) \\ C^*_{y_{lf}} &= C_{y_{lf}} cos(\delta) + C_{x_{lf}} sin(\delta) \\ C^*_{y_{rf}} &= C_{y_{rf}} cos(\delta) + C_{x_{rf}} sin(\delta) \\ B_{o,21} = (-\frac{w}{2} C^*_{x_{lf}} + a C^*_{y_{lf}}); B_{o,22} &= (\frac{w}{2} C^*_{x_{rf}} + a C^*_{y_{rf}}) \\ B_{o,23} = (-\frac{w}{2} C_{x_{lr}} - b C_{y_{lr}}); B_{o,24} &= (\frac{w}{2} C_{x_{rr}} - b C_{y_{rr}}) \end{aligned} \tag{5.3.12}$$

The affine control effectiveness matrix B_Δ is constructed by simply replacing the linear tire stiffness parameters within B_o with their affine counterparts as

$$B_\Delta = B_o(C_{x_{ij}} \to \Delta C_{x_{ij}}, C_{y_{ij}} \to \Delta C_{y_{ij}}) \tag{5.3.13}$$

It is our goal to select a vector Δu which best generates the virtual force vector v requested by the reference tracking controller. As the system is over actuated we may add secondary objectives and formulate the optimization problem stated as

$$\begin{aligned} & \underset{x}{\text{minimize}} && f_0(x) \\ & \text{subject to} && f_i(x) \leq b_i, \; i = 1, \ldots, m. \end{aligned} \tag{5.3.14}$$

In this framework, we are attempting to select the optimal decision variable x which minimizes the objective function f_o while obeying the constraint equations f_i.

With the adopted affine representation, our decision variable is Δu, a desired change in slip-ratios with respect to current operating slip-ratios. We propose the least square objective function

$$f_o(\Delta u) = ||W_v(B_o u_o + B_\Delta \Delta u - v_d)||_2^2 + \lambda ||W_u(u_o + \Delta u)||_2^2 + \xi ||W_{\Delta u} \Delta u||_2^2 \tag{5.3.15}$$

with Tikhonov and smoothing regularization [37]. The first Euclidean norm of the objective function penalizes error between desired and actual generalized virtual forces. The matrix W_v is a diagonal matrix, who's entries weigh the relative irritation from error in respective virtual forces. The second Euclidean norm represents irritation to tire slip-ratio. The diagonal matrix W_u provides a means to weigh the irritation of allocating slip-ratio to each respective tire. For the currently described controller, W_u is an identity matrix of appropriate size. The first two terms of the objective function make the statement: *Select the* Δu *which best achieves the desired virtual forces, while minimizing* $\sigma_{lf}^2 + \sigma_{rf}^2 + \sigma_{lf}^2 + \sigma_{rr}^2$. The final term of the objective function represents irritation to changes in slip-ratio Δu. This term provides a means of smoothing the solution of the optimal control allocation problem. The diagonal matrix $W_{\Delta u}$ provides a means to weigh the relative irritation of changes in slip-ratio at each respective tire. The scalar parameters λ and ξ provide a means to proportion the relative importance of the objectives of each normative term. In practice they are parameters which are tuned by a calibration engineer.

It is desirable that slip-ratios requested by the optimal allocation controller be constrained to avoid excessive saturation of the tires. However, this constraint is intrinsically induced by the affine approximation of tire forces introduced in Eqns. (5.3.6) and (5.3.7). Specifically, excessive slip ratio requests will be discouraged by negative affine slopes ΔC_x contained in the control effectiveness matrix B_Δ. In addition, the optimal allocation controller will seek to avoid excessively degrading lateral force generation implied by Figure 5.2.2 in an attempt to achieve the desired lateral virtual force ΣF_y. Finally, if multiple solutions satisfy the virtual force requests, the solution with minimum Euclidean norm of vector u will be selected as a result of the second term of the objective function. For these reasons, no extrinsic constraint equations f_i are imposed on the optimal allocation controller.

The objective function stated in Eqn. (5.3.15) can be expanded and transformed to the quadratic form

$$f_o(\Delta u) = \frac{1}{2}\Delta u^T H \Delta u + f^T \Delta u + b \tag{5.3.16}$$

where

$$\begin{aligned} H &= 2[B_\Delta^T W_v B_\Delta + \lambda W_u + \xi W_{\Delta u}] \\ f^T &= 2[(B_o u_o - v_d)^T W_v B_1 + \lambda u_o^T W_u] \\ b &= [(B_o u_o - v_d)^T W_v (B_o u_o - v_d) + \lambda u_o^T W_u u_o] \end{aligned} \tag{5.3.17}$$

The optimal solution to this unconstrained quadratic objective function can be determined utilizing the optimality condition for unconstrained problems [37]

$$\nabla f_o(\Delta u) = 0 \tag{5.3.18}$$

analytically as

$$\Delta u^* = -2[H + H^T]^{-1} f \tag{5.3.19}$$

where Δu^* is the optimal solution.

In summary, the optimal control allocation technique takes advantage of the affine approximation of tire force generation stated in Eqns. (5.3.6) and (5.3.7) to select a desired slip-ratio vector (Eqn. (5.3.1)) which will best achieve the desired generalized virtual force vector (Eqn. (5.3.2)). As a result of the objective function stated in Eqn. (5.3.15), the optimal allocation controller intrinsically respects the saturating nature of the tires, and settles upon an optimal solution without the use of extrinsic constraint equations. The control allocation technique developed in this section is not implementable due to the infeasibility of estimating some affine tire parameters. However, it will serve as a benchmark to the performance of the sub-optimal, but realizable allocation controllers to be developed in the subsequent sections.

5.3.2 Sub-Optimal Control Allocation

In order to reduce the aforementioned optimal control allocation problem to a real time implementable control allocation problem relying upon only estimates of longitudinal tire stiffness $\hat{C}_x$, the following assumptions are made:

- Negligible steering angle:
    - $\cos(\delta) \to 1$
    - $\sin(\delta) \to 0$
- Small slip-ratio approximation:
    - $\Delta C_x \to C_x$
    - $C_y, \Delta C_y \to 0$

The small slip-ratio approximation is of particular interest. First, it states that for small slip-ratios the affine slope of the longitudinal force generation curve is approximately equal to its linear slope. This intuition is conveyed graphically in Figure 5.2.1. Additionally it states that for small slip-ratios, selection of slip ratio has little effect on lateral force generation. This conjecture can be verified graphically in Figure 5.2.2.

In effect, the small slip-ratio assumption has removed the ability of control allocation to attempt to achieve desired lateral forces, and thus the virtual force vector for the problem is reduced to

$$v^T = [\Sigma F_x, \Sigma M_y] \tag{5.3.20}$$

Additionally, the affine representation of tire force generation has been reduced to the linear approximation

$$F_{x_{ij}} \approx C_{x_{ij}} \sigma_{ij} \tag{5.3.21}$$

With these approximations, the affine control effectiveness relationship of Eqn. (5.3.8) can be reduced to the linear relationship

$$v = Bu \tag{5.3.22}$$

with control effectiveness matrix B provided as

$$B = \begin{bmatrix} \hat{C}_{x_{LF}} & \hat{C}_{x_{RF}} & \hat{C}_{x_{LR}} & \hat{C}_{x_{RR}} \\ -\frac{w}{2}\hat{C}_{x_{LF}} & \frac{w}{2}\hat{C}_{x_{RF}} & -\frac{w}{2}\hat{C}_{x_{LR}} & \frac{w}{2}\hat{C}_{x_{RR}} \end{bmatrix} \tag{5.3.23}$$

It is important to note that the only tire information required in the control effectiveness matrix is the easily estimated longitudinal stiffness $\hat{C}_x$.

The sub-optimal control allocation objective function is proposed as

$$f_o(u) = ||W_v(Bu - v_d)||_2^2 + \lambda||W_u u||_2^2 + \xi||W_{\Delta u}(u - u_o)||_2^2 \tag{5.3.24}$$

where the decision variable is u, as opposed to the decision variable Δu used by the optimal allocation controller. The objectives of Eqn. (5.3.24) are similar to those of Eqn. (5.3.15). The first term penalizes error between desired and actual virtual forces, the second term penalizes allocation of independent slip-ratios and the final term penalizes changes in slip-ratios from their previous values.

Eqn. (5.3.24) can be expanded, resulting in the quadratic form

$$f_o(u) = \frac{1}{2}u^T H u + f^T u + b \tag{5.3.25}$$

where

$$\begin{aligned} H &= 2[B^T W_v B + \lambda W_u + \delta W_{\Delta u}] \\ f^T &= 2[-v_d^T W_v B - \delta u_o^T W_{\Delta u}] \\ b &= [v_d^T W_v v_d + \delta u_o^T W_{\Delta u} u_o] \end{aligned} \tag{5.3.26}$$

It is tempting to solve for the unconstrained solution to this problem as was done with the optimal control allocation problem. However, doing so would result in infeasible slip-ratio requests. While the optimal control allocation problem intrinsically included the saturating nature of tires as well as the coupling between lateral force degradation and slip-ratio, the sub-optimal control allocation formulation does neither.

Instead, it is necessary to extrinsically impose constraints on the sub-optimal control allocation problem. It is desired that each tire's slip-ratio should be constrained between some minimum and maximum value

$$\sigma_{min} \leq \sigma_{ij} \leq \sigma_{max} \tag{5.3.27}$$

which can be formulated as a linear matrix inequality as

$$\underbrace{\begin{bmatrix} I_{4\times4} \\ -I_{4\times4} \end{bmatrix}}_{A} u \leq \underbrace{\begin{bmatrix} 1_{4\times1}\sigma_{max} \\ -1_{4\times1}\sigma_{min} \end{bmatrix}}_{b} \tag{5.3.28}$$

Eqns. (5.3.25) and (5.3.28) constitute a quadratic programming problem with many available solution methods. We select Hildreth's Quadratic Programming procedure for simplicity [38].

5.3.3 Fuzzy Inference Adaptation

In the previous section, the optimal control allocation problem was simplified by a small slip-ratio assumption to produce a sub-optimal, but real-time implementable control allocation routine. Unfortunately, in doing so information regarding the saturating nature of physical tires as well as the coupling between slip-ratio and lateral force degradation was lost. In this section, a simple holistic is proposed to regain some of this lost information, resulting in a real time implementable controller which approaches the performance of the optimal control allocation problem. The holistic is as follows: *as a tire becomes saturated, its longitudinal stiffness becomes reduced.*

This statement can be verified by Figure 5.3.2, which highlights the estimated longitudinal stiffness for both rear tires of a prototype wheel-motored vehicle when launched on a split-μ surface. For this experiment, the left tires of the vehicle were operating on dry pavement, while the right tires were operating on a wet tile surface with significantly lower friction coefficient μ. The same amount of torque was input at both wheels, which intuitively would result in a higher level of saturation experienced by the tire operated on the lower-μ surface. As is evident from the figure, the intuitively more saturated right-rear tire returns a notably smaller estimate of longitudinal stiffness as compared with the left-rear tire operating on dry pavement. It therefore follows that allocation of additional slip-ratio to a tire experiencing decreased longitudinal stiffness should be discouraged.

Fortunately, the objective function of the sub-optimal control allocation problem, provided in Eqn. (5.3.24) enables just such penalization. Entries of the diagonal matrix W_u represent the irritation of allocating slip-ratio to the corresponding tire. For example, a larger value of the diagonal entry of W_u corresponding to σ_{rf} will discourage allocation of

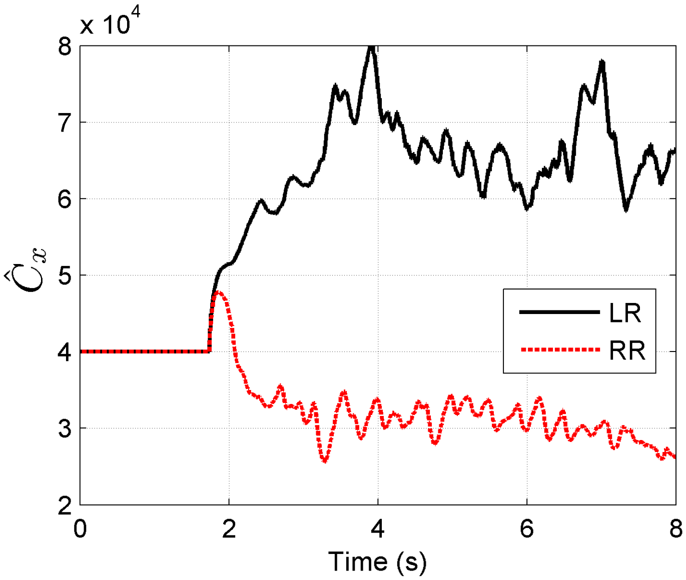

Figure 5.3.2: Longitudinal Stiffness Estimate $\hat{C}_x$ During Vehicle Launch with Right Tire on Low-μ Surface

slip-ratio to the right front tire. Thus, the entries of W_u should be adapted as follows

$$W_u = \begin{bmatrix} \eta_{lf} & 0 & 0 & 0 \\ 0 & \eta_{rf} & 0 & 0 \\ 0 & 0 & \eta_{lr} & 0 \\ 0 & 0 & 0 & \eta_{rr} \end{bmatrix} \tag{5.3.29}$$

where the η_{ij} entries obey the following fuzzy rule base:

- If $\hat{C}_{x_{ij}}$ is Small then η_{ij} is Large ($\eta_{ij} \triangleq \eta_{large}$)
- If $\hat{C}_{x_{ij}}$ is Large then η_{ij} is Small ($\eta_{ij} \triangleq 1$)

and where $\eta_{large} \gg 1$ is a constant to be selected by the calibration engineer.

However, as tires progressively lose grip with the road surface, the classification of saturation should be a continuous function, as proposed in Figure 5.3.3. A tire operating with an estimated longitudinal stiffness $\hat{C}_x \leq 1 \times 10^4$ is classified as fully saturated. Conversely, a tire operating with $\hat{C}_x \geq 4 \times 10^4$ is classified as non-saturated. The presented membership

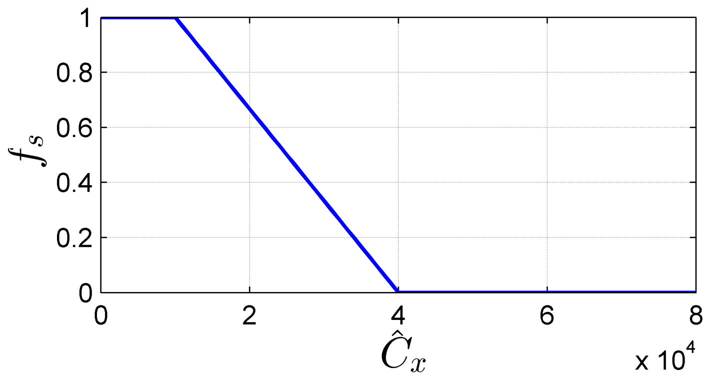

Figure 5.3.3: Membership Function for “Saturated” Tire

function was arrived upon via simulation and experimental testing, but it is the prerogative of the calibration engineer to tailor the function for individual needs.

Using singleton fuzzification, product composition and inference, and centroid defuzzification [25], the expression for η_{ij} is given by:

$$\eta_{ij} = f_s(\hat{C}_{x_{ij}}) + \eta_{large}(1 - f_s(\hat{C}_{x_{ij}})) \tag{5.3.30}$$

The proposed fuzzy membership based saturation function restores some of the information originally lost due to the small slip-ratio assumption. For example, as a tire becomes saturated its longitudinal stiffness decreases and the penalization of allocating slip-ratio to that tire increases. This increased penalization effectively constrains the maximum slip-ratio which will be allocated to a given tire. Much like with the optimal allocation controller, this constraint on slip-ratio is intrinsic within the objective function. For this reason, the extrinsic constraints required by the previously introduced sub-optimal control allocation problem are unnecessary for the currently discussed allocation problem. Thus, with a correctly selected fuzzy membership function, an analytical solution to the objective function presented in Eqn. (5.3.25) can be generated as

$$u^* = -2[H + H^T]^{-1} f \tag{5.3.31}$$

avoiding the necessity for iterative solution routines.

5.4 Comparative Simulation Study

Three control allocation problems have been developed in the previous sections. The first is deemed infeasible for practical implementation, but is to serve as a benchmark for the performance of subsequent systems. This controller shall be termed *Optimal* in simulation results. The next control allocation problem was made realizable by instituting a small slip-ratio assumption. This controller will be termed *Static* as it utilizes an unchanging control effector penalization matrix W_u. The final control allocation problem discussed utilizes a fuzzy membership function to adapt the control effector penalization matrix, penalizing allocation of slip-ratio to saturated tires. This controller shall be termed *Adaptive.* These three control allocation problems are implemented within the architecture introduced in Section 2.2 and simulated in the CarSim© simulation environment for the purpose of performance comparison.

The open loop sine-with-dwell steering maneuver based on the U.S. Department of Transportation's electronic stability control systems testing method FMVSS-126, presented in Figure 5.4.1, was applied to the CarSim© vehicles while traveling at $80kph$. When applied to a vehicle without stability control functionality this maneuver resulted in loss of control. The *optimal*, *static* and *adaptive* systems where tasked with allocating desired slip-ratio to stabilize the vehicle, while attempting to impart zero net longitudinal force (off throttle driver input). Slip-ratio control and longitudinal force estimation was implemented utilizing the logic developed in Chapter 4. The optimal allocation controller obtained virtual yaw moment and net lateral force requests from a reference tracking controller attempting to track the yaw rate and lateral acceleration of a linear 2 degree of freedom bicycle model [7]. The adaptive and static controllers received only the virtual yaw moment request, as the lateral coupling was removed as a result of the small slip-ratio assumption. All three controllers

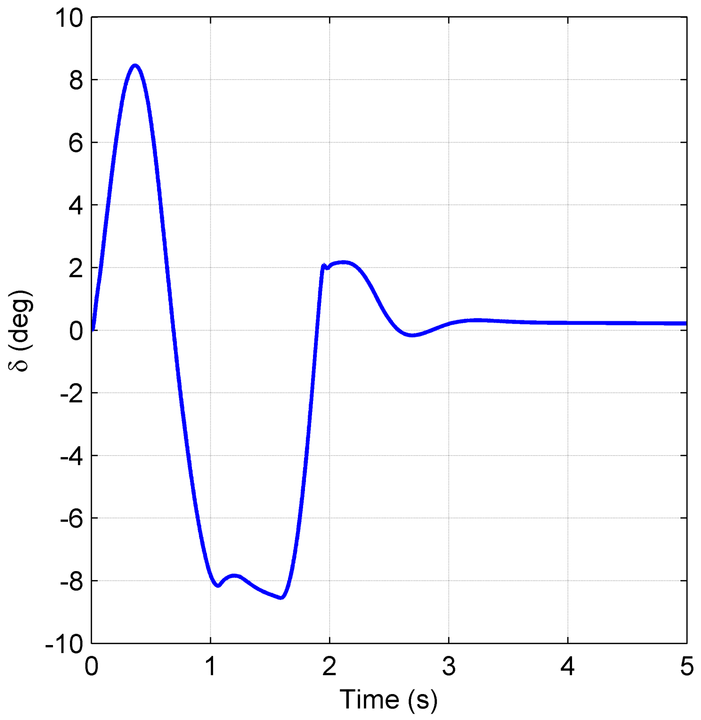

Figure 5.4.1: Sine-with-Dwell Open-Loop Steering Angle, Measured at the Front Wheels

were able to stabilize the vehicle.

Figure 5.4.2 compares the desired virtual forces with those achieved by each allocation controller. The net longitudinal forces and yaw moments achieved by the three controllers are quite similar. However, the net lateral forces achieved by the three controllers are notably different. In general, the static controller exhibits much larger discrepancy from the desired lateral force as compared with the optimal and adaptive controllers. This should be unsurprising as the static controller makes no attempt to achieve the desired virtual lateral force. The adaptive controller also does not attempt to achieve the desired virtual lateral force, but approaches the performance of the optimal controller by penalizing slip-ratio allocation to saturated tires. By avoiding requesting increased slip-ratios from already saturated tires, the adaptive controller avoids unnecessary degeneration of lateral tire force. The result of which is evident when comparing the trajectories of the three controlled vehicles in Figure 5.4.3. From the figure it is evident that the trajectory of the adaptive controller

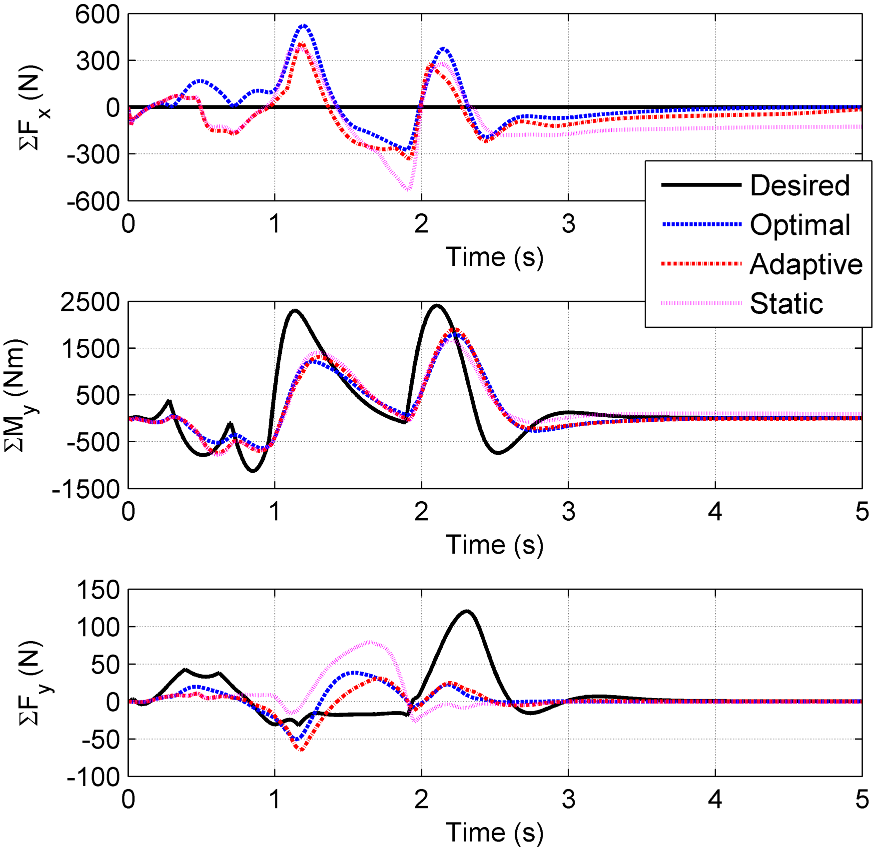

Figure 5.4.2: Desired and Achieved Generalized Forces During Sine-with-Dwell Maneuver

approaches the trajectory of the optimal control system.

This simulation study has shown the capabilities of the control allocation architecture when applied with the purpose of vehicle stability control. The *optimal* system highlights the potential performance if the controller had use of a detailed model of tire force generation. However, as this model cannot be known during practical operation, two realizable systems, *Static* and Adaptive were developed. This simulation study showcases how the performance of the *Adaptive* system approaches that of the *Optimal* system. This result is favorable, especially as the *Adaptive* system is practically implementable.

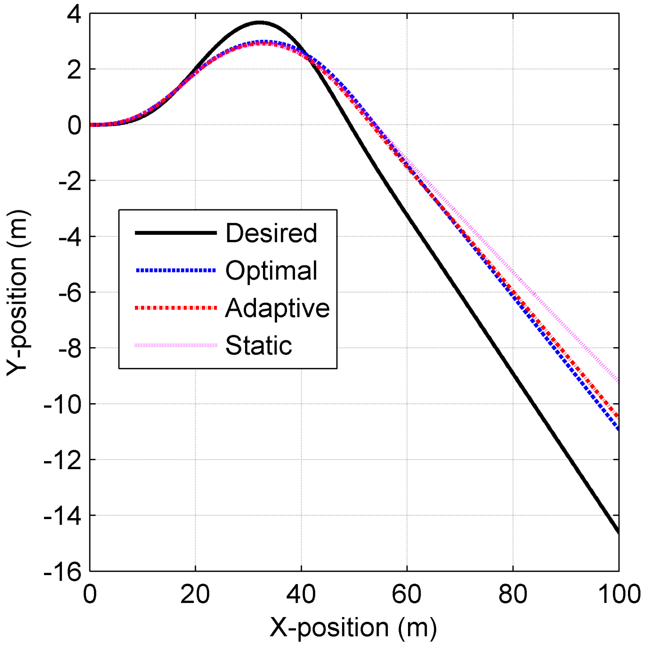

Figure 5.4.3: Trajectory Resulting from Steer-with-Dwell Maneuver

5.5 Experimental Validation

A prototype vehicle with hub-electric motors installed at each rear wheel was utilized for experimental validation. The control system implemented on the vehicle included the slip-ratio controller developed in Chapter 4 in conjunction with the sub-optimal control allocation problem with fuzzy inference adaptation. Data from two experimental tests will be presented.

5.5.1 Low-μ Launch

The vehicle was subjected to full throttle launch from rest on a surface with very low coefficient of friction. The goal of this testing was to validate the intrinsic constraint of slip-ratio resulting from the fuzzy membership function presented in Figure 5.3.3. The study was conducted with different values of η_{large} as defined in Eqn. (5.3.30). $\eta_{large} = 50$ employed modest penalization for allocation of slip-ratio to saturated tires, while $\eta_{large} = 1000$ much more aggressively penalized slip-ratio allocation to saturated tires.

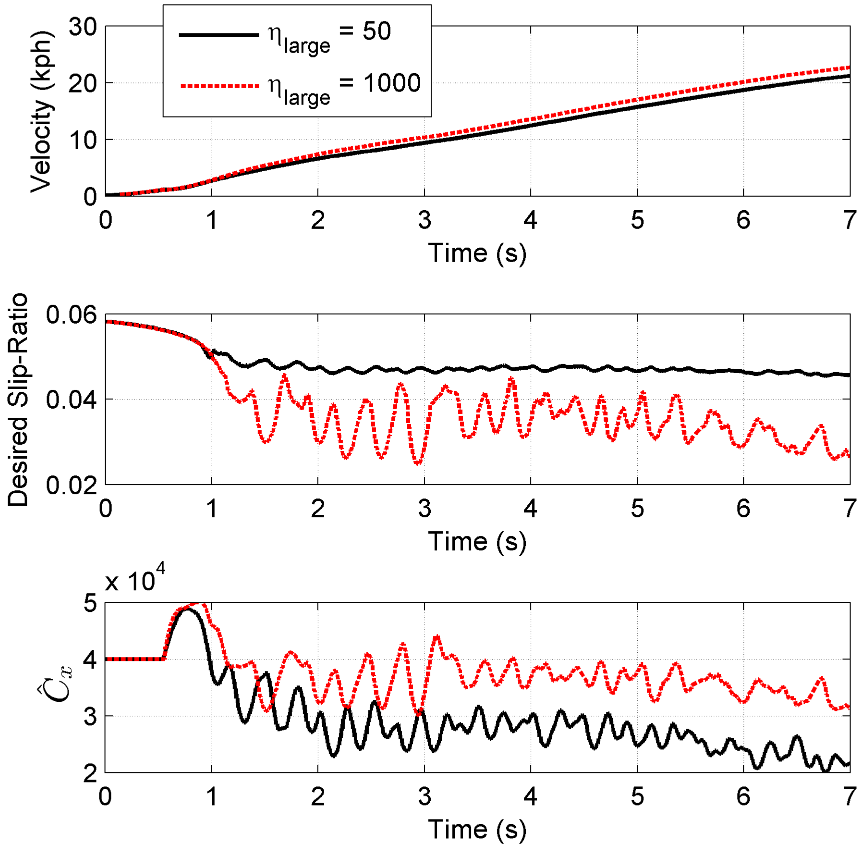

Figure 5.5.1: Experimental Full Throttle Launch on Low-μ Surface

The result of these two experiments is shown in Figure 5.5.1. From the figure it is evident that reasonable slip-ratio was requested in each situation, validating the hypothesized intrinsic constraint of slip-ratio. The larger value of penalization coefficient η_{large} results in a more dramatic reduction in slip-ratio allocation request in response to estimated longitudinal stiffness $\hat{C}_x$. As a result of this more conservative slip-ratio allocation, the $\eta_{large} = 1000$ study was able to constrain the vehicle tires to a region of higher longitudinal stiffness. All in all, when initialized with $\eta_{large} = 1000$ the vehicle was able to accelerate to $20kph$ in 25% less time than the comparable vehicle initialed with $\eta_{large} = 50$.

5.5.2 Split-μ Launch

The first term of the objective function of Eqn. 5.3.24 penalizes error between the desired and allocated virtual forces ΣF_x and ΣM_y. The weighting matrix

$$W_v = \begin{bmatrix} w_{\Sigma F_x} & 0 \\ 0 & w_{\Sigma M_y} \end{bmatrix} \tag{5.5.1}$$

allows for independently prescribed irritation to error in allocation of each respective virtual force. For this experiment, the irritation to error in allocated yaw moment was set to $w_{\Sigma M_y} = 10$ and the irritation to error in allocated longitudinal force $w_{\Sigma F_x}$ was varied. The experiment was conducted during a full throttle launch on a split-μ surface, where the left tires were on pavement and the right tires were on a very slippery surface. The control allocation problem was tasked with attempting to generating a very large virtual longitudinal force ΣF_x while at the same time generating zero total yaw-moment ΣM_y. Figure 5.5.2 shows the resulting experimental data.

It is evident from the figure that changing the relative weight between the elements in matrix W_v has a large effect on the performance of the vehicle. With roughly equivalent weighting, the allocation problem compromises on maximum longitudinal force generated in order to minimize developed yaw-moment. However, when the weighting of $w_{\Sigma F_x}$ is one order of magnitude larger than $w_{\Sigma M_y}$, the allocation problem much more aggressively achieves longitudinal force at the cost of generating a large yaw-moment error. This resulted in much faster vehicle acceleration, but required driver steering input to counteract the undesirable yaw-moment.

The purpose of this experiment was not to determine which ratio of weights was decidedly better. Instead, it was to show that the control allocation framework provides an intuitive method for calibrating vehicle performance. Indeed, the ratio of the elements in W_v can be calibrated as a function of vehicle speed and other metrics to provide the desired compromise

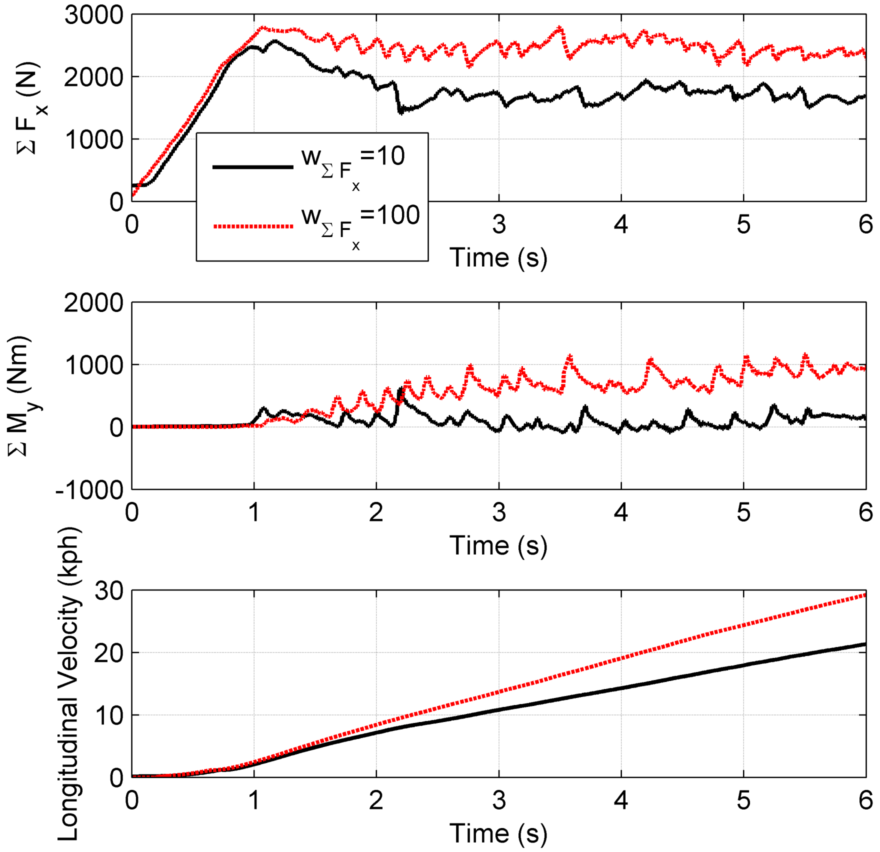

Figure 5.5.2: Experimental Full Throttle Launch on Split-μ Surface

between virtual force allocation for all vehicle maneuvers.

5.6 Summary of Slip-Ratio Allocation

Control allocation is tasked with allocating slip-ratio requests to each wheel-motored corner of the vehicle in an attempt to achieve the desired vehicle performance. In this chapter, three control allocation problems were introduced. First, the optimal control allocation problem was introduced, which relied on unknowable tire information to provide a benchmark for physically achievable performance. This optimal problem was then made practically implementable by instituting a small slip-ratio assumption. However, with this assumption, the control allocation problem became sub-optimal as it no longer incorporated the saturating nature of physical tires in its decisions. In an attempt to regain some knowledge of tire saturation, a third control allocation problem was presented, which utilized a fuzzy membership function to identify saturated tires and penalize allocation of control effort to those tires. It was shown with simulation that the performance of this sub-optimal controller with fuzzy membership adaptation approached that of the optimal controller.

The sub-optimal control allocation problem with fuzzy membership adaptation was validated on an experimental vehicle with wheel-motors installed at each rear wheel. It was shown that the system did in fact adapt its behavior, intrinsically avoiding excessive tire saturation on low-μ surfaces. In addition, it was shown that the control allocation framework provides an intuitive method of calibrating planar vehicle performance.

Chapter 6

Conclusion

6.1 Summary and Conclusions

The goal of this dissertation work was to develop a philosophy for the control of planar vehicle dynamics for a wheel-motored vehicle. To this end, it was proposed that control decisions should be made in the slip-ratio domain. This decision allowed for the intrinsic and explicit constraint of slip-ratio, helping to avoid excessive tire saturation and improve vehicle performance. For practical implementation, the control philosophy required development of three novel control modules:

1. As slip-ratio cannot be directly measured, it must instead be estimated. This dissertation work proposes such an estimator which is developed to utilize only sensors currently available on modern production automobiles. The estimator is novel in its incorporation of a body-fixed rigid-body dynamics model to ensure accurate estimation during cornering maneuvers. Additionally, the estimator relies upon a fuzzy membership function to ascertain whether certain measurements are usable.

2. A slip-ratio controller was developed to modulate wheel-motor torques in an effort to achieve desired slip-ratios. This dissertation work proposed the novel implementation of a disturbance observer for this task. Such an implementation leverages the known

wheel-motor torque generation to estimate the longitudinal force developed by the tire. This information is then used to make the slip-ratio controller robust to changing road surface and tire condition.

3. Combining the estimated slip-ratio with the estimated longitudinal force developed by the tire, it is possible to ascertain longitudinal tire stiffness. This information is leveraged to improve allocation accuracy but also – utilizing a fuzzy membership model of tire saturation – to penalize allocation of slip-ratio to saturated tires. The result is a control allocation framework which allocates slip-ratio requests to wheel-motored corners of the vehicle to best achieve the desired planar vehicle dynamics while at the same time minimizing tire saturation.

The three control modules developed in this work were implemented on an B-class vehicle with its conventional powertrain replaced by wheel-motors installed at each rear wheel. Utilizing this vehicle, the functionality of the independent control modules and the control architecture as a whole was validated. The result was an intuitively calibrated system which automatically adapted its behavior to changing road conditions. Such a system should pave the way towards safer and better handling vehicles.

6.2 Future Directions

The controllers developed in this work made the assumption that wheel torques were solely generated by the wheel-motor systems. However, it is likely that these systems may have to operate in parallel with electro-hydraulic brake systems for mass production implementation. Together, these systems provide necessary redundancy, as well as an increase in the maximum braking torque. It is a proposed topic of future investigation to develop a cooperative strategy for the implementation of the wheel-motor in parallel with the brake system. The control allocation framework proposed in this work can be easily expanded to incorporate additional actuators. However, the slip-ratio controller developed in this work strongly relied upon knowledge of the input wheel torque. With the incorporation of a less precisely known brake torque, this controller may require revision.

The planar state estimator developed in this work was satisfactory for preliminary testing, but suffered from error during extended braking. During braking, the system integrates Inertial Measurement Unit (IMU) sensors to estimate vehicle state. However, during prolonged braking, the alignment errors in acceleration measurement due to road grade as well as chassis pitch and roll resulted in large state estimate errors. It is suggested that this IMU misalignment be compensated to improve state estimate during braking maneuvers. One suggested direction of research would incorporate intermittent Global Positioning System (GPS) data to correct drift and alignment error experienced by the IMU system.

References

[1] Injury prevention and control: Motor vehicle saftey, Vol. 2013, Centers of Disease Control and Prevention, www.cdc.gov/motorvehiclesafety/statecosts, 2011.

[2] Statistical analysis of the effectiveness of electronic stability control (esc) systems: Final report, Tech. rep., U.S. Department of Transportation National Highway Traffic Safety Administration (2007).

[3] Federal motor vehicle safety standards electronic stability control systems controls and displays, Tech. rep., Department of Transportation: National Highway and Traffic Safety Administration (2007).

[4] W. Manning, D. Crolla, A review of yaw rate and sideslip controllers for passenger vehicles, Transactions of the Institute of Measurement and Control 29 (2) (2007) 117–135.

[5] L. Wei, Y. Hai, R. McGee, K. Ming, J. Medanic, Vehicle pure yaw moment control using differential tire slip, in: American Control Conference, 2009. ACC '09., 2009, pp. 3331–3336.

[6] S. Murata, Innovation by in-wheel-motor drive unit, Vehicle System Dynamics 50 (6) (2012) 807–830.

[7] D. Karnopp, Body-fixed coordinate formulation, in: Vehicle Stability, Marcel Dekker, 2004, pp. 106–109.

[8] K. Bayar, J. Wang, G. Rizzoni, Development of a vehicle stability control strategy for a hybrid electric vehicle equipped with axle motors, Proceedings of the Institution of Mechanical Engineers, Part D: Journal of Automobile Engineering 226 (6) (2012) 795–814.

[9] S. Varnhagen, M. O. Anubi, D. Margolis, Development of realizable and adaptive wheel torque allocation for the control of planar vehicle dynamics, in: ASME (Ed.), Dynamic Systems and Control, San Antonio, Texas, 2014.

[10] H. B. Pacejka, Chapter 4 - semi-empirical tyre models, in: H. B. Pacejka (Ed.), Tyre and Vehicle Dynamics (Second Edition), Butterworth-Heinemann, Oxford, 2006, pp. 156–215.

[11] C. B. Patil, R. G. Longoria, J. Limroth, Control prototyping for an anti-lock braking control system on a scaled vehicle, in: Decision and Control, 2003. Proceedings. 42nd IEEE Conference on, Vol. 5, 2003, pp. 4962–4967 Vol.5.

[12] S. Varnhagen, D. Margolis, Longitudinal slip ratio control of electric powertrains using a controller output observer for disturbance rejection, SAE International Journal of Passenger Cars - Mechanical Systems 7 (1) (2014) 65–72.

[13] C. R. Carlson, J. C. Gerdes, Nonlinear estimation of longitudinal tire slip under several driving conditions, in: American Control Conference, 2003. Proceedings of the 2003, Vol. 6, 2003, pp. 4975–4980 vol.6.

[14] J. Farrelly, P. Wellstead, Estimation of vehicle lateral velocity, in: Control Applications, 1996., Proceedings of the 1996 IEEE International Conference on, 1996, pp. 552–557.

[15] T. A. Wenzel, K. J. Burnham, M. V. Blundell, R. A. Williams, Dual extended kalman filter for vehicle state and parameter estimation, Vehicle System Dynamics 44 (2) (2006) 153–171.

[16] J. Villagra, B. d'Andrea Novel, M. Fliess, H. Mounier, Estimation of longitudinal and lateral vehicle velocities: An algebraic approach, in: American Control Conference, 2008, 2008, pp. 3941–3946.

[17] K. Kobayashi, C. C. Ka, K. Watanabe, Estimation of absolute vehicle speed using fuzzy logic rule-based kalman filter, in: American Control Conference, Proceedings of the 1995, Vol. 5, 1995, pp. 3086–3090 vol.5.

[18] D. C. Karnopp, D. L. Margolis, R. C. Rosenberg, Body-fixed coordinates, in: System Dynamics: Modeling and Simulation of Mechatronic Systems, Fourth Edition, Wiley, Hoboken, New Jersey, 2006, pp. 109–114.

[19] J. Lu, T. Brown, Method and apparatus for compensating misalignments of a sensor system used in a vehicle dynamic control system US6782315 B2.

[20] H. Eric Tseng, L. Xu, D. Hrovat, Estimation of land vehicle roll and pitch angles, Vehicle System Dynamics 45 (5) (2007) 433–443.

[21] B. D. Anderson, J. B. Moore, Optimal Filtering, Prentice-Hall Inc., Englewood Cliffs, New Jersey, 1979.

[22] G. Welch, G. Bishop, An introduction to the kalman filter, Tech. rep., University of North Carolina at Chapel Hill (2006).

[23] R. Kandepu, B. Foss, L. Imsland, Applying the unscented kalman filter for nonlinear state estimation, Journal of Process Control 18 (78) (2008) 753–768.

[24] P. J. Antsaklis, A. N. Michel, A Linear Systems Primer, Birkhauser, Boston, 2007.

[25] L.-X. Wang, A Course in Fuzzy Systems and Control, Prentice-Hall International, 1997.

[26] Y. Jong-Hwa, P. Huei, A cost-effective sideslip estimation method using velocity measurements from two gps receivers, Vehicular Technology, IEEE Transactions on 63 (6) (2014) 2589–2599.

[27] D. M. Bevly, R. Jihan, J. C. Gerdes, Integrating ins sensors with gps measurements for continuous estimation of vehicle sideslip, roll, and tire cornering stiffness, Intelligent Transportation Systems, IEEE Transactions on 7 (4) (2006) 483–493.

[28] B. Ozkan, D. Margolis, M. Pengov, The controller output observer: Estimation of vehicle tire cornering and normal forces, Journal of Dynamic Systems, Measurement, and Control 130 (6) (2008) 061002–061002.

[29] T. Umeno, Y. Hori, Robust speed control of dc servomotors using modern two degrees-of-freedom controller design, Industrial Electronics, IEEE Transactions on 38 (5) (1991) 363–368.

[30] L. Ho Seong, M. Tomizuka, Robust motion controller design for high-accuracy positioning systems, Industrial Electronics, IEEE Transactions on 43 (1) (1996) 48–55.

[31] K. Ohishi, Realization of fine motion control based on disturbance observer, in: Advanced Motion Control, 2008. AMC '08. 10th IEEE International Workshop on, 2008, pp. 1–8.

[32] K. Ohishi, T. Miyazaki, K. Inomata, H. Yanagisawa, D. Koide, H. Tokumaru, Robust tracking servo system considering force disturbance for the optical disk recording system, Industrial Electronics, IEEE Transactions on 53 (3) (2006) 838–847.

[33] G. F. Franklin, D. J. Powell, A. Emami-Naeini, Tustin's method, in: Feedback Control of Dynamic Systems, Fifth Edition, Pearson Prentice Hall, New Jersey, 2006, pp. 606–609.

[34] M. Tomizuka, Zero phase error tracking algorithm for digital control, Journal of Dynamic Systems, Measurement, and Control 109 (1) (1987) 65–68.

[35] T. A. Johansen, T. I. Fossen, Control allocationa survey, Automatica 49 (5) (2013) 1087–1103.

[36] J. Villagra, B. dAndra Novel, M. Fliess, H. Mounier, A diagnosis-based approach for tireroad forces and maximum friction estimation, Control Engineering Practice 19 (2) (2011) 174–184.

[37] S. Boyd, L. Vandenberghe, Regularization, in: Convex Optimization, Cambridge University Press, 2004, pp. 306–308.

[38] L. Wang, Hildreth's quadratic programming procedure, in: Model Predictive Control System Design and Implementation Using MATLAB, 2009, pp. 63–68.